

Morphological Control of Copper and Cuprous Oxide Nanoparticles via Synthesis  
and Oxidation/Reduction Reactions

by

Ryan Mowbray

B.S. United States Coast Guard Academy, 2009

*A thesis submitted to the*

*Faculty of the Graduate School of the*

*University of Colorado in partial fulfillment*

*of the requirement for the degree of*

*Master of Science*

*Department of Chemical and Biological Engineering*

*2013*

*This thesis entitled:*

*Morphological Control of Copper and Cuprous Oxide Nanoparticles via Synthesis and  
Oxidation/Reduction Reactions*

*written by Ryan William Mowbray*

*has been approved for the Department of Chemical and Biological Engineering*

*Mark Stoykovich*

---

*Will Medlin*

---

*Date 16 April 2013*

*The final copy of this thesis has been examined by the signatories, and we  
Find that both the content and the form meet acceptable presentation standards  
Of scholarly work in the above mentioned discipline.*

*Mowbray, Ryan William (M.S., Chemical Engineering)*

*Morphological Control of Copper and Cuprous Oxide Nanoparticles via Synthesis and Oxidation/Reduction Reactions*

*Thesis directed by Assistant Professor Mark P. Stoykovich*

## **Abstract**

*Morphological structure at the nanoscale dictates material properties due to size and shape dependent effects which are not present in bulk materials. In this work, novel synthetic routes are presented for the synthesis of copper nanoparticles including cubes, octahedra and platelets which could find applications in catalysis and sensing applications. In addition, intermediate morphology of copper/cuprous oxide nanoparticles during reduction by hydrogen gas are characterized by UV-Vis spectroscopy and TEM imaging. The results of the UV-Vis characterization show that nanoparticle oxide reduction occurs by a different mechanism than reduction in the bulk due to short diffusion lengths and high metal diffusivity. The results of this work may be applied to the fields of catalysis, sensing, plasmonics, and spectroscopy where improved control of structure at the atomic level leads to improved functionality.*

## Contents

- I. Introduction
- II. Shape Control of Cu<sub>2</sub>O Nanoparticles via Oxidation Conditions
  - a. The formation of hollow nanoparticles by the oxidation or sulfidation of metal nanospheres which become hollow due to the nanoscale Kirkendall effect has been investigated. In this work a generalized kinetic diffusion model for the formation of hollow nanoparticles is developed and combined with experimental data for the Cu/Cu<sub>2</sub>O nanoparticle system to yield industrially relevant diffusion parameters.
- III. Intermediate Morphology of Cu/Cu<sub>2</sub>O Nanoparticles During Reduction by H<sub>2</sub>
  - a. In-Situ UV-Vis characterization is used to monitor the reduction of Cu<sub>2</sub>O nanoparticles to Cu by hydrogen gas. Comparison of observed spectra to Mie scattering predictions are used to show that the reaction proceeds via a different mechanism for nanoparticles than in bulk oxides.
- IV. Shape Control of Cu Nanoparticles via Ligand Selection
  - a. Novel synthetic routes are developed which lead to copper cubes, octahedra, and platelets. These synthesis routes are unique in that a single procedure produces markedly different shapes by changing only the coordinating ligand between oleic acid (cubes), tetradecylphosphonic acid (octahedral), and stearic acid (platelets).
- V. Conclusion

Appendix A: Review of the Optical Properties of Noble Metals

## FIGURES

## Figure

1.	<i>Intermediate state of Cu/Cu<sub>2</sub>O nanoparticle through oxidation</i>	6
2.	<i>Scaled radii vs. scaled time</i>	7
3.	<i>Contour maps of <math>a_f</math> and <math>A</math> without surface energy</i>	8
4.	<i>TEM micrographs of Cu<sub>2</sub>O nanoparticles</i>	9
5.	<i>Temperature dependence of full oxidation time <math>t_{full}</math></i>	10
6.	<i>Linearized diffusivity parameters vs. <math>T</math></i>	11
7.	<i>Contour maps of <math>a_f</math> and <math>A</math> with surface energy</i>	12
8.	<i>Linearized diffusivity parameters vs. <math>T</math> with surface energy</i>	14
9.	<i>Three-layered optical model</i>	18
10.	<i>Raw Mie scattering spectra</i>	19
11.	<i>Predicted UV-Vis Spectra</i>	20
12.	<i>Predicted spectra for Cu shell, Cu<sub>2</sub>O core</i>	21
13.	<i>Average reduction time vs. temperature</i>	22
14.	<i>Diffusion model particle geometry</i>	23
15.	<i>Plot of non-dimensional radius vs. time</i>	25
16.	<i>Synthetic scheme for Cu cubes, platelets, and octahedra</i>	30
17.	<i>TEM micrographs for Cu cubes, platelets, and octahedra</i>	31
18.	<i>(100) and (111) facets of Cu</i>	32
19.	<i>Sequential oxidation of Cu nanocube</i>	36
20.	<i>Cu nanocube oxidation in solution</i>	37

## Chapter I - Introduction

Copper is a unique metal which has historically been valued because it has a high electrical conductivity, high thermal conductivity, and low cost. Chemically, it can exist in many different forms with oxidation states of 0, +1, and +2 which are referred to as copper, cuprous, and cupric respectively. Recently copper has found numerous applications in the field of nanotechnology where nanostructured copper-based materials have been used in printed electronics<sup>1</sup>, catalysts for the water-gas-shift reaction methanol synthesis<sup>2</sup>, and in transparent conducting films<sup>3</sup>. The common theme of these applications is that structure at the nanoscale dictates the properties of a system. With that in mind the focus of this work is on developing novel methods to control and characterize the structure of copper and copper oxide nanoparticles by first varying synthetic conditions to achieve shape control, and by varying oxidation and reduction conditions to post-synthetically modify the morphology of the particles.

This work heavily relies on the unique optical properties of copper nanoparticles. But what exactly is the origin of these special properties and why is copper different from other elements? To answer this question we look to the electronic structure of the noble metals gold, silver, and copper which make up group 11 of the periodic table. All three group 11 elements have an electronic structure which includes a full D orbital and one electron in the highest energy S orbital. The result of this configuration is a “free” S electron which forms a sea of electrons which flows throughout the lattice structure of the material and gives rise to the high conductivity of the metal via metallic bonding<sup>4</sup>. The D electrons behave in a manner similar to bound electrons in other non-conducting materials<sup>4</sup>. They exist in orbitals which are held close to their central atom and may be excited to higher energy orbitals upon interaction with an incoming high energy photon. Thus, we encounter a dichotomy of interactions with photons: low energy photons interact with the free conduction electrons and cause transitions within the continuous conduction band, and high energy photons interact with the bound D electrons which cause electronic transitions at discrete energy levels.

For copper nanoparticles, there is an overlapping region where both bound and free electron interactions are significant which lays around 2.2 eV<sup>5</sup> and gives rise to some of the interesting properties discussed later in this work. This region is altered further with the introduction of size-dependent surface scattering effects which become significant at dimensions which approach the mean free path of conduction electrons for a material<sup>6</sup>, or around 50 nm for copper<sup>5</sup>. As a result, nanoparticles in this size range exhibit a unique phenomenon known as a plasmon resonance. At a particular wavelength of light, incident photons oscillate in phase with conduction band electrons at the surface of the particle and an intense, sharp absorption peak is observed, leading to large increases in the local electric field surrounding the nanoparticle<sup>5</sup>. The two primary effects of the resonance, large sharp absorbance peaks and increased local electric field give rise to useful applications in spectroscopy<sup>7,8</sup> and catalysis<sup>9,10</sup>. If the geometry or size of the copper particle is altered such that the plasmon resonance occurs near the 2.2 eV boundary where bound electron contributions become significant, the net effect is to reduce the magnitude of the plasmon resonance due to dampening effects from interband transitions<sup>5</sup>. In this way, size and shape control are critically important for the practical application of copper nanoparticles in

plasmonic applications. For a more detailed treatment of the optical properties of noble metals and their origin, see Appendix A.

Previous work performed by our lab has demonstrated the usefulness of the localized surface plasmon resonance as a tool to study the oxidation of copper nanoparticles. First, it was shown that the behavior of the LSPR peak of Cu nanoparticles oxidizing in solution is highly dependent on whether or not the solvent contains  $\pi$  bonds, which effectively quench the plasmon resonance by donating electrons to the surface of the nanoparticle. Upon oxidation, an insulating shell forms which prevents the quenching effect and drastically increases the LSPR peak. This effect was not observed for solvents which did not contain  $\pi$  bonds (cyclohexane, chloroform, etc.)<sup>11</sup>. Next, the behavior of copper nanoparticle films during oxidation at various temperatures was characterized by monitoring the oxidation in-situ at various temperatures using a heated UV-Vis setup. This investigation found that low temperature nanoparticle oxidation exhibited different behavior than what would otherwise be expected from extrapolated bulk values which were calculated from experimental data taken on thin films at  $<700\text{K}$ . In addition, this work demonstrated that Cu nanoparticles are subject to the nanoscale Kirkendall effect during oxidation, which causes the particles to become hollow because of a large difference in diffusivity between oxygen and copper at the metal/oxide interface<sup>12</sup>.

The present thesis is devoted to expanding on the previous work on our lab and developing novel ways to control and identify the morphology of nanostructured copper and copper oxide systems. Our long term goal is to fully characterize the effect of oxidation and reduction conditions on particle morphology and localized surface plasmon resonance and to characterize synthetic conditions which lead to novel and unique nanostructured copper and copper oxide materials.

Chapter 2 summarizes the results of a model which was developed using the thermodynamic extremal principle<sup>13,14</sup> with the goal of tuning oxidation conditions in order to achieve precise shape control of cuprous oxide nanoparticles. The model demonstrates the ability to tune the final void radius of cuprous oxide nanoparticles as a function of the initial copper nanoparticle radius. In addition, this model was combined with experimental oxidation data to calculate diffusivity parameters for the Cu/Cu<sub>2</sub>O system.

Chapter three covers an investigation into the intermediate morphology of copper/copper oxide nanoparticles during reduction by hydrogen gas at elevated temperatures. Previous studies on transition metal oxide nanoparticle reduction did not discuss intermediate morphology due to the limitations of the equipment used and therefore required application of bulk mechanisms in order to extract useful parameters such as activation energy and rate constants. In our work, we used UV-Vis spectroscopy combined with Mie scattering modeling to show that nanoparticle oxide reduction operates by an entirely different mechanism than bulk oxide reduction due to the small diffusion lengths and high diffusivity induced by the highly strained Cu/Cu<sub>2</sub>O interface.

Chapter four discusses our progress to date on synthetic shape control of copper nanoparticles. Starting with standard nanoparticle synthesis recipes, we drastically increased the ligand to copper precursor

ratios in order to induce shape control using various ligands. Thus far we have demonstrated the ability to synthesize cubes, octahedral, and platelets.

Finally, the conclusions and future work to be accomplished in the Cu/Cu<sub>2</sub>O nanoparticle system are presented in chapter 5.

## References

- (1) Yabuki, A.; Arriffin, N. *Thin Solid Films* 2010, 518, 7033.
- (2) Campbell, C. T.; Daube, K. A. *Journal of Catalysis* 1987, 104, 109.
- (3) Rathmell, A. R.; Bergin, S. M.; Hua, Y.-L.; Li, Z.-Y.; Wiley, B. J. *Advanced Materials* 2010, 22, 3558.
- (4) Ehrenreich, H.; Philipp, H. R. *Physical Review* 1962, 128.
- (5) Wang, H.; Tam, F.; Grady, N. K.; Halas, N. J. *Journal of Physical Chemistry B Letters* 2005, 109, 18218.
- (6) Averitt, R. D.; Westcott, S. L.; Halas, N. J. *Journal of the Optical Society of America B* 1999, 16, 1824.
- (7) Pastoriza-Santos, I.; Sanchez-Iglesias, A.; Rodriguez-Gonzalez, B.; Liz-Marzan, L. M. *Small* 2009, 5, 440.
- (8) Tao, A.; Sinsermsuksakul, P.; Yang, P. *Angew. Chem. Int. Ed.* 2006, 45, 4597.
- (9) Cho, H.-J.; Hwang, P.-G.; Jung, D. *Journal of Physics and Chemistry of Solids* 2011, 72, 1462.
- (10) Zhou, X.; Gan, Y.; Sun, S. *Acta Physica-Chimica Sinica* 2012, 28, 2071.
- (11) Rice, K. P.; Walker, E. J. J.; Stoykovich, M. P.; Saunders, A. E. *Journal of Physical Chemistry C*. 2011, 115, 1793.
- (12) Rice, K. P.; Paterson, A. S.; Stoykovich, M. P. 2013, *submitted*.
- (13) Svoboda, J.; Turek, I.; Fisher, F. *Philosophical Magazine* 2005, 85, 3699.
- (14) Svoboda, J.; Fischer, F.; Vollath, D. *Acta Materialia* 2009, 57, 1912.



# Chapter II – Shape Control of Cu<sub>2</sub>O Nanoparticles via Oxidation

## 1. Introduction

The ability to control morphology of nanoparticle systems is a useful and practical tool for controlling the behavior of novel materials. One example of this approach is the formation of hollow nanoparticles by the oxidation or sulfidation of metal nanospheres which become hollow due to the nanoscale Kirkendall effect [1]. Some materials that have been shown to form hollow nanostructures by this mechanism include copper oxide [2-4], cobalt sulfide [1,5], iron oxide [6], aluminum oxide [2], and zinc oxide [7] among many others. Hollow nanostructures are useful to improve the catalytic performance of some catalysts by increasing their porosity and surface area [8,9]. In addition, hollow iron oxide nanospheres have been demonstrated for use as drug delivery systems by using the void as a way to deliver specific drug payloads to sites of interest [10,11]. A common thread among both of these applications for hollow nanoparticles is the need to precisely control the void size and final particle morphology in order to optimize the process.

Previous work by Svoboda et al. [12] demonstrated the development of a model for the formation of a binary phase hollow nanosphere from a metallic nanosphere. In this model, a metal nanoparticle undergoing a reaction with a non-metallic component (i.e. oxidation, sulfidation, etc.) is assumed to have an intermediate geometry similar to Fig. 1, and the hollow void size is determined by the diffusivity in each layer. In their work, the authors showed that the model could be developed using the thermodynamic extremal principle [13] to derive quantitative expressions for the kinetics of this system. They use characteristic values of the Cu/Cu<sub>2</sub>O system while assuming  $D_{Cu \text{ in } Cu}$  is greater than  $D_{Cu \text{ in } Cu_2O}$  and neglecting surface energy to demonstrate that the model is roughly consistent with experimental evidence for full oxidation time. However they didn't show explicitly the relation between the void size and the diffusivities of the Cu/Cu<sub>2</sub>O system.

In this work it is our aim to expand Svoboda and coworkers' model to show the relationship between the void size, full oxidation time and the diffusivities for the Cu/Cu<sub>2</sub>O nanoparticle system which includes surface energy and makes no prior assumptions regarding the relative magnitude of the diffusivities in the system. Additionally, the model will extract quantitative and experimentally useful diffusivity parameters for the Cu/Cu<sub>2</sub>O system by combining the expanded model with experimental data. The resulting model demonstrates the effects of surface energy on the system and quantifies exactly how hollow nanoparticle formation is dependent on the diffusivities of the system.

## 2. Experimental

Copper nanoparticles were synthesized as previously described in [14,15]. Oxidation of the particles from solid Cu to hollow Cu<sub>2</sub>O was performed at various temperatures and monitored by in-situ UV-Vis

spectroscopy as outlined previously in [14]. Briefly, thin films of Cu nanoparticles were prepared in a nitrogen glove box by evaporation of a colloidal suspension of monodisperse Cu nanoparticles in hexane on a clean glass slide. The thin films were removed from the nitrogen environment and immediately heated to various temperatures while simultaneously being monitored by UV-Vis spectroscopy using an Ocean Optics USB-4000 spectrometer. Oxidation time was characterized by the disappearance of the plasmon resonance peak at approximately 600 nm.

Hollow void size was characterized by TEM and processed with ImageJ software to find particle and void areas. In this procedure, particle and void areas were directly measured from TEM images. Void and particle diameters were then calculated by assuming a spherical geometry and calculating the diameter from the particle's area. The oxide particle volume was determined from the calculated diameter and used to find the initial particle volume using the molar volume ratio between Cu<sub>2</sub>O and Cu. Finally, the ratio of the void radius to the initial copper radius was found by comparing the final and initial volumes of Cu<sub>2</sub>O and Cu.

### 3. Theory

#### 3.1. Model Parameters

For clarity, the parameters of the model previously presented by Svoboda et al. and expanded upon in this work are presented in this section. The geometry of the system is assumed to take the form of Fig. 1 where  $a$  is the hollow void radius,  $\rho$  is the metal core radius, and  $R$  is the metal oxide shell radius and all are normalized to the initial nanoparticle radius  $R_0$ . Time  $t$  is scaled by a characteristic time constant  $\tau_{MX} \equiv R_g T R_0^2 / D_{MX} |\Delta g_{MX}|$  where  $R_g$  is the gas constant,  $T$  is temperature,  $D_{MX}$  is the diffusivity of metal in the metal oxide, and  $\Delta g_{MX}$  is the change in Gibbs free energy for the oxidation reaction. Material dependent properties in the system include  $u$ ,  $v$ ,  $\Omega$ , and  $f$ , where  $u$  and  $v$  are the molar fraction of metal and oxygen in metal oxide respectively,  $\Omega$  is the molar volume ratio of metal and metal oxide, and  $f$  is the geometric correlation factor. For the Cu/Cu<sub>2</sub>O system  $u = 2/3$ ,  $v = 1/3$ ,  $\Omega = 7.11/7.90$ , and  $f = 0.7815$ .  $\gamma_a$ ,  $\gamma_\rho$ , and  $\gamma_R$  are the normalized surface energies at the interfaces  $a$ ,  $\rho$ , and  $R$  respectively. The input parameters in the model are the diffusivity of metal in the metal oxide phase:  $D_{MX}$ , the diffusivity of oxygen in the metal oxide phase:  $D_{XX}$ , and the self-diffusivity of metal in the metal phase:  $D_{MM}$ . In this work, the diffusivity parameters are normalized and presented as  $D_{MX}^{XX} \equiv D_{XX} / D_{MX}$  and  $D_{MX}^{MM} \equiv D_{MM} / D_{MX}$ . In the following sections we show that these characteristic diffusivities determine the kinetics of the system.

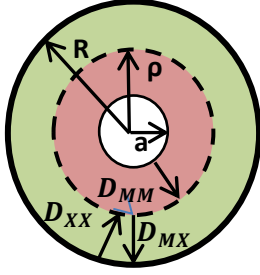


**Figure 1: Intermediate state of the nanoparticle through oxidation. For this figure  $a$  is the hollow void radius,  $\rho$  is the metal core radius, and  $R$  is the metal oxide shell radius and all are normalized to the initial nanoparticle radius  $R_0$ .**

### 3.2. Model Solution

The model gives a system of differential equations by following the derivation of Svoboda et al. except in this case we use the independent variables  $a$  and  $\rho$  from the beginning instead of  $\rho$  and  $R$ . This system of differential equations describes the oxidation of a Cu/Cu<sub>2</sub>O nanoparticle system by describing the radii  $a$ ,  $\rho$ , and  $R$  vs. time.

$$\begin{bmatrix} \left[ \frac{fu}{D_{MX}^{MM}} \left( \frac{1}{a} - \frac{1}{\rho} \right) + \frac{1}{\Omega} \left( \frac{1}{\rho} - \frac{1}{R} \right) \right] a^4 & -\frac{1-u\Omega}{\Omega} \left( \frac{1}{\rho} - \frac{1}{R} \right) a^2 \rho^2 \\ -\frac{1-u\Omega}{\Omega} \left( \frac{1}{\rho} - \frac{1}{R} \right) a^2 \rho^2 & \left[ \frac{(1-u\Omega)^2}{\Omega} + \frac{uv\Omega}{D_{MX}^{XX}} \right] \left( \frac{1}{\rho} - \frac{1}{R} \right) \rho^4 \end{bmatrix} \begin{bmatrix} \dot{a} \\ \dot{\rho} \end{bmatrix} = \begin{bmatrix} a^2 \left( 1 - \frac{2\gamma_a u \Omega}{a} - \frac{2\gamma_R}{R} \right) \\ \rho^2 \left( -1 - \frac{2\gamma_\rho u \Omega}{\rho} + \frac{2\gamma_R (1-u\Omega)}{R} \right) \end{bmatrix} \quad (1)$$

$$R = \left( \frac{1+a^3-(1-u\Omega)\rho^3}{u\Omega} \right)^{\frac{1}{3}} \quad (2)$$

If  $a \neq 0$  and  $\rho \neq 0$ , the determinant of the matrix in Eq. (1) is always positive.

$$Det = a^4 \rho^4 \left( \frac{1}{\rho} - \frac{1}{R} \right) \left[ \left( \frac{f(1-u\Omega)^2}{D_{MX}^{MM}\Omega} + \frac{fuv\Omega}{D_{MX}^{MM}D_{MX}^{XX}} \right) \left( \frac{1}{a} - \frac{1}{\rho} \right) + \frac{v}{D_{MX}^{XX}} \left( \frac{1}{\rho} - \frac{1}{R} \right) \right] \quad (3)$$

Since Eq. (3) is positive, the inverse matrix exists and the following system of differential equations is given.

$$\dot{a} = \left( \frac{v\Omega}{D_{MX}^{XX}} - (1-u\Omega) - \frac{2\gamma_a}{a} \left[ (1-u\Omega)^2 + \frac{uv\Omega^2}{D_{MX}^{XX}} \right] - \frac{2\gamma_\rho(1-u\Omega)}{\rho} - \frac{2\gamma_R v \Omega}{RD_{MX}^{XX}} \right) \frac{a^2 \rho^4}{Det} \left( \frac{1}{\rho} - \frac{1}{R} \right) \quad (4)$$

$$\dot{\rho} = \left( - \left[ \frac{f}{D_{MX}^{MM}} \left( \frac{1}{a} - \frac{1}{\rho} \right) + 1 \right] - \frac{2\gamma_a(1-u\Omega)}{a} - \frac{2\gamma_\rho}{\rho} \left[ \frac{fu\Omega}{D_{MX}^{MM}} \left( \frac{1}{a} - \frac{1}{\rho} \right) + 1 \right] + \frac{2\gamma_R f(1-u\Omega)}{RD_{MX}^{MM}} \left( \frac{1}{a} - \frac{1}{\rho} \right) \right) \frac{a^4 \rho^2}{Det} \left( \frac{1}{\rho} - \frac{1}{R} \right) \quad (5)$$

The solution of this system of equations gives  $a$  and  $\rho$  as a function of time and is dependent on characteristic values of the metal/metal oxide system. This system of differential equations may be solved numerically using a 4th order Runge-Kutta method. Specifically, the integration was performed using the MATLAB non-stiff low order ordinary differential equation solver ode45. Input parameters to the solver were a relative tolerance of  $10^{-6}$  and an absolute tolerance of  $10^{-5}$ .

## 4. Results and Discussion

### 4.1. Without Surface energy

To simplify the solution methods and to obtain a first approximation for the behavior of this system which is consistent with the results of Svoboda et al., surface energies are assumed to be negligible;  $\gamma_a = \gamma_\rho = \gamma_R = 0$ . Eqs. (4)-(5) are solved as described in section 3.2 to yield a plot of the radii vs. time as shown in Fig. 2. Hereafter the characteristic values of the Cu/Cu<sub>2</sub>O system are used for  $u, v, \Omega$ , and  $f$ .  $a_f$  is the final hollow radius and  $A$  is the final scaled time.

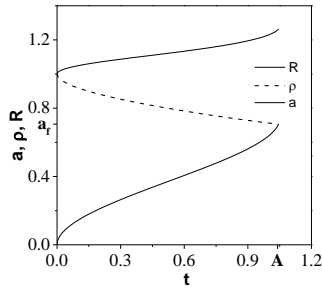


**Figure 2: Scaled radii  $a, \rho, R$  vs. Scaled time  $t$ . For this example,  $D_{MX}^{XX}$  and  $D_{MX}^{MM}$  are taken as 0.01 and 0.05, respectively. The resulting hollow radius and scaled oxidation time are  $a_f = 0.71$  and  $A = 1.0$ .**

When the values of  $D_{MX}^{XX}$  and  $D_{MX}^{MM}$  change in Eqs. (4)-(5), the resulting  $a_f$  and  $A$  change accordingly. Therefore  $a_f$  and  $A$  are considered to be functions of  $D_{MX}^{XX}$  and  $D_{MX}^{MM}$ . Using the method outlined above, Eqs. (4)-(5) were solved for all values of  $D_{MX}^{XX}$  and  $D_{MX}^{MM}$ , and the assembly of solutions were plotted as a contour of  $a_f$  and  $A$  with  $D_{MX}^{XX}$  and  $D_{MX}^{MM}$  as the independent variables as in Fig. 3(a)-(b). Reformulating the two independent variables by normalizing with  $D_{XX}$  and  $D_{MM}$  as  $\tau_{XX} \equiv R_g T R_o^2 / D_{XX} |\Delta g_{MX}|$ ,  $D_{XX}^{MM} \equiv D_{MM} / D_{XX}$ ,  $D_{XX}^{MX} \equiv D_{MX} / D_{XX}$  and  $\tau_{MM} \equiv R_g T R_o^2 / D_{MM} |\Delta g_{MX}|$ ,  $D_{MM}^{MX} \equiv D_{MX} / D_{MM}$ ,  $D_{MM}^{XX} \equiv D_{XX} / D_{MM}$  and using the same integration steps yield the contour shown in Fig. 3(c)-(d) and Fig. 3(e)-(f) respectively. The independent variables are reformulated in the three columns of Fig. 3 in order to identify regions of interest for the system from which we can extract useful parameters. For example, in the region of large values of  $D_{MX}^{MM}$ , the contours of  $a_f$  in Fig. 3(a) are nearly vertical and  $A$  in Fig. 3(b) is nearly constant. Combining these two parameters in the large  $D_{MX}^{MM}$  region allows for the determination of  $D_{MX}, D_{XX}$  within the large  $D_{MX}^{MM}$  region as described below. On the other hand, Fig. 3(a) and (b) are not useful for small values of  $D_{MX}^{MM}$  since the contours of  $a_f$  are not vertical and  $A$  is not constant. Instead, it is possible to use Fig. 3(e) and (f) where we can use a similar process in the large  $D_{MX}^{XX}$  region which corresponds to the small  $D_{MX}^{MM}$  region in Fig. 3(a)-(b), since the contours of  $a_f$  in Fig. 3(e) are nearly vertical and  $A$  in Fig. 3(f) is nearly constant in that region, which enables the determination of  $D_{XX}, D_{MM}$  as described below.

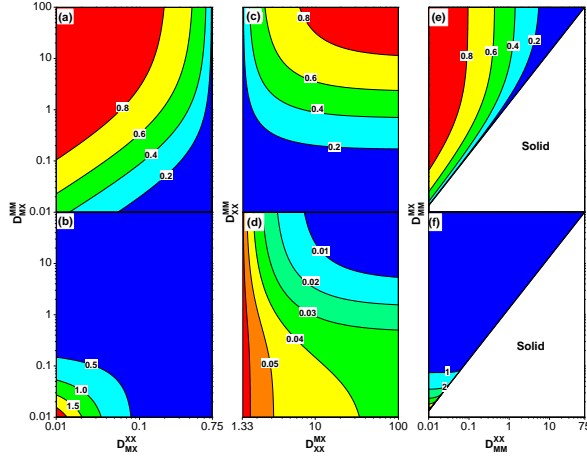


**Figure 3: Contour maps of  $a_f$  (a), (c), (e) and  $A$  (b), (d), (f) without surface energy. Oxidized NPs become hollow in  $D_{MX}^{XX} < 0.75$  and solid in  $D_{MX}^{XX} \geq 0.75$  for (a)-(b), hollow in  $D_{XX}^{MX} > 4/3$  and solid in  $D_{XX}^{MX} \leq 4/3$  for (c)-(d), hollow in  $D_{MM}^{XX} < 0.75 D_{MM}^{MX}$  and solid in  $D_{MM}^{XX} \geq 0.75 D_{MM}^{MX}$  for (e)-(f).**

Analysis of the contour plots reveals three general rules for the formation of hollow nanoparticles. First, in agreement with Eq. (4), the contour plot shows that oxidation results in a hollow particle only when  $v\Omega/D_{MX}^{XX} - (1 - u\Omega) > 0$  since  $\dot{a}$  must be positive in order for the void to grow. This requirement appears in all the contour plots shown in Fig. 3 where  $D_{MX}^{XX} < 0.75$  for Fig. 3(a)-(b),  $D_{XX}^{MX} > 4/3$  for Fig. 3(c)-(d), and  $D_{MM}^{XX} < 0.75 D_{MM}^{MX}$  for Fig. 3(e)-(f). These three conditions are equivalent, but are expressed in terms of the different independent variables consistent with the contour plots in Fig. 3. Second, for a given  $D_{MX}^{MM}$  value,  $D_{MX}^{XX}$  varies inversely with  $a_f$ , which is consistent with the general model of the nanoscale Kirkendall effect since a larger difference in the diffusivity between the two species in the binary phase leads to a larger void size [1]. Third, for a fixed value of  $D_{MX}^{XX}$ , void radius is positively related to  $D_{MX}^{MM}$ . This is in contrast to previous discussions of the nanoscale Kirkendall effect, which assumed that the ratio of the diffusivities within the binary phase was the only contributing factor to the size of the hollow void [1]. We hypothesize that this is because lower values of  $D_{MX}^{MM}$  slow down the supply of copper to the  $\text{Cu}_2\text{O}$  shell and also inhibit the growth of the void in the center of the particle. These three properties taken together show that  $D_{MX}^{XX}$  has an absolute upper limit for the formation of hollow nanoparticles, and within that limit, all three characteristic diffusivities of the system are important for determining final void size.

Moving on from general trends to specific parameter extraction we use experimental data combined with the contour plots in Fig. 3 to extract diffusion values for the Cu/ $\text{Cu}_2\text{O}$  system. TEM images of the oxidized Cu nanoparticles were analyzed in accordance with the procedure given in section 2 and showed that  $a_f$  varies with temperature as shown in Fig. 4(a)-(c):  $a_f = 0.65$  at  $100^\circ\text{C}$ ,  $0.55$  at  $150^\circ\text{C}$ , and  $0.50$  at  $200^\circ\text{C}$ . These experimental  $a_f$  values constrain the diffusivity parameters to a single line within the contour plot from the upper right to the lower left in Fig. 3(a). Since a single observable  $a_f$  isn't enough to specify the exact values of  $D_{MX}^{XX}$  and  $D_{MX}^{MM}$  in the contour plot, we investigate the limiting

behavior on these  $a_f$  lines in two regions of interest in Fig. 3(a), the upper right corner (Region I) and the lower left corner (Region II).

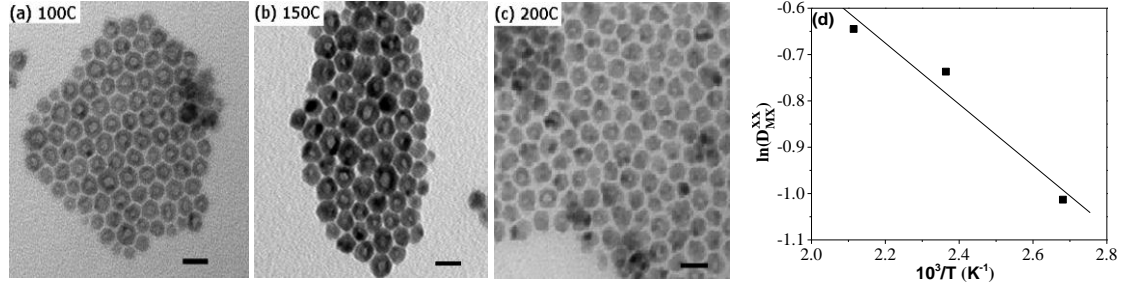


**Figure 4:** Transmission electron micrographs of Cu/Cu<sub>2</sub>O particles heated for 1 hr in air at (a) 100°C, (b) 150°C, and (c) 200°C. The average hollow radius  $a_f$  is (a) 0.65, (b) 0.55, and (c) 0.50. All scalebars correspond to 20 nm. (d)  $D_{MX}^{XX}$  vs.  $T$  based on Region I in Fig. 3(a).

#### 4.1.1. Region I

Region I is the area of Fig. 3(a) where  $D_{MX} \ll D_{MM}$  and the contour lines are almost vertical. In other words, on these  $a_f$  lines,  $a_f$  doesn't vary with  $D_{MX}^{MM}$ . Therefore, the experimental  $a_f$  lines specify the value of  $D_{MX}^{XX}$  at each temperature. In order to extract diffusivity values in this region, we assume a functional form of diffusivity  $D = D_0 \exp(-E_d/R_g T)$  and use the  $D_{MX}^{XX}$  value at  $D_{MX}^{MM} = 100$  on each  $a_f$  line for approximation, then  $D_{MX}^{XX} = 0.36$  at 100°C, 0.48 at 150°C, and 0.52 at 200°C. Using these three values, a linearized diffusivity equation was plotted and fit with a least squares algorithm to find the pre-exponential factor and diffusion energy as in Fig. 4(d),

$$D_{MX}^{XX} = D_{Cu in Cu_2O}^{O in Cu_2O} = 2.2 \exp(-5.5/R_g T) \quad (6)$$

Within the same region of Fig. 3(b) we find that  $A$  is nearly constant, therefore we may use the same value of  $D_{MX}^{XX}$  and  $D_{MX}^{MM}$  used for calculating Eq. (6) to find  $A = 0.0671$  at 100°C, 0.0688 at 150°C, and 0.0697 at 200°C. Concurrently, in-situ UV-Vis data gives full oxidation times of  $t_{full} = 335$ (sec) at 100°C, 79.5(sec) at 150°C, and 37.5(sec) at 200°C as in Fig. 5(a) [14]. Recall from the model derivation  $t_{full}/\tau_{MX} = A$  and  $\tau_{MX} \equiv R_g T R_0^2 / D_{MX} |\Delta g_{Cu_2O}|$ . Substituting the exponential form of diffusivity  $D_{MX}$  and linearizing leads to  $\ln(t_{full}/TA) = E_{MX}/R_g T + \ln(R_g R_0^2 / D_{0MX} |\Delta g_{Cu_2O}|)$ . Here  $R_g$  is  $8.314 \times 10^{-3}$  kJ/mol/K,  $R_0$  is 5.5 nm which is given by TEM images of Fig. 4 (a)-(c) and  $|\Delta g_{Cu_2O}|$  is 47 kJ/mol. Substituting in experimental  $t_{full}$  and performing a linear fit on a plot of  $\ln(t_{full}/TA)$  vs.  $1/T$  as in Fig. 5(b) yields

$$D_{MX} = D_{Cu in Cu_2O} = 53 \exp(-36.4 / R_g T) \text{ (nm}^2/\text{s)} \quad (7)$$

Then using  $D_{0XX}/D_{0MX} = 2.2$ ,  $E_{XX} - E_{MX} = 5.5$  from Eq. (6) gives

$$D_{XX} = D_{O in Cu_2O} = 120 \exp(-42/R_g T) \text{ (nm}^2/\text{s)} \quad (8)$$

To recap, using Fig. 3(a)-(b), experimental values of oxidation time and hollow radius, and the assumption of  $D_{MX} \ll D_{MM}$ ,  $D_{MX}$  and  $D_{XX}$  were found explicitly as functions of temperature. In the next section, we apply a similar strategy to find diffusivity parameters for other regions of interest in Fig. 3.

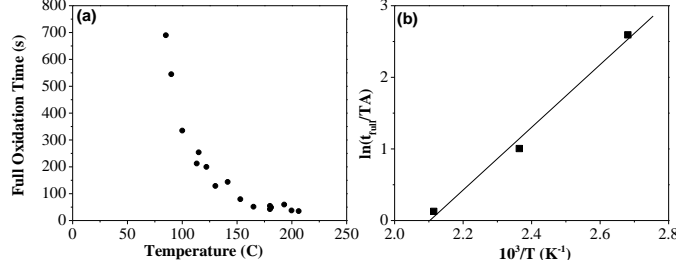


**Figure 5: (a) The temperature dependence of the full oxidation time  $t_{full}$  [14]. (b)  $t_{full}$  vs.  $T$  based on Region I in Fig. 3(b).**

#### 4.2.2. Region II

Region II exists in the far right side of Fig. 3(c)-(d) where  $D_{XX} \ll D_{MX}$  and  $D_{MM} \ll D_{MX}$ . Through the use of Fig. 3(c)-(d) and methods similar to those used for Region I,  $D_{MM}$  and  $D_{XX}$  may be calculated. Fig. 3(c)-(d) is appropriate for this analysis because  $A$  is nearly constant in Fig. 3(d) along each  $a_f$  line, and  $a_f$  doesn't vary with  $D_{XX}^{MX}$  in Fig. 3(c). Similarly to Region I, using experimental  $a_f$  values and assuming  $D_{XX}^{MX} = 100$ ,  $D_{XX}^{MM}$  is equal to 3.3 at 100°C, 1.7 at 150°C, and 1.3 at 200°C. Using these  $D_{XX}^{MM}$  and  $D_{XX}^{MX}$  values in Fig. 3(d),  $A$  is equal to 0.013 at 100°C, 0.019 at 150°C, and 0.022 at 200°C. Combining these data points and linearizing in the same manner as shown above gives  $D_{XX}^{MM}$ ,  $D_{XX}$ , and  $D_{MM}$  by least squares fitting to a linearized plot in Fig. 6(a)-(b) to produce:

$$D_{XX}^{MM} = D_{OinCu_2O}^{CuinCu} = 0.035 \exp(14/R_g T) \quad (9)$$

$$D_{XX} = D_{OinCu_2O} = 90 \exp(-43/R_g T) \text{ (nm}^2/\text{s)} \quad (10)$$

$$D_{MM} = D_{CuinCu} = 3.2 \exp(-29/R_g T) \text{ (nm}^2/\text{s)} \quad (11)$$

The same process may be applied to region II in Fig. 3(e)-(f) which results in nearly identical values for  $D_{XX}$  and  $D_{MM}$  as in Fig. 6(c)-(d).

$$D_{MM}^{XX} = D_{CuinCu}^{OinCu_2O} = 29 \exp(-14/R_g T) \quad (12)$$

$$D_{MM} = D_{CuinCu} = 4.9 \exp(-29/R_g T) \text{ (nm}^2/\text{s)} \quad (13)$$

$$D_{XX} = D_{OinCu_2O} = 140 \exp(-43/R_g T) \text{ (nm}^2/\text{s)} \quad (14)$$

Thus far  $D_{MX}$  and  $D_{XX}$  have been calculated assuming  $D_{MX} \ll D_{MM}$ , and  $D_{MM}$  and  $D_{XX}$  have been calculated assuming  $D_{XX} \ll D_{MX}$  and  $D_{MM} \ll D_{MX}$ . These two conditions represent the two limiting conditions in the Fig. 3 contour plots, but the resulting  $D_{XX}$  value is nearly the same regardless of the

region from which it was calculated. Therefore we can expect that  $D_{XX}$  takes similar value in all regions of Fig. 3 for realistic values of  $a_f$  and  $A$ . On the other hand we have no evidence from which to infer whether the Cu/Cu<sub>2</sub>O system operates closer to Region I or Region II which makes it difficult to determine whether our calculated  $D_{MX}$  or  $D_{MM}$  is realistic. Fortunately, going back to the beginning and including surface energy with the model provides further insight into this question.

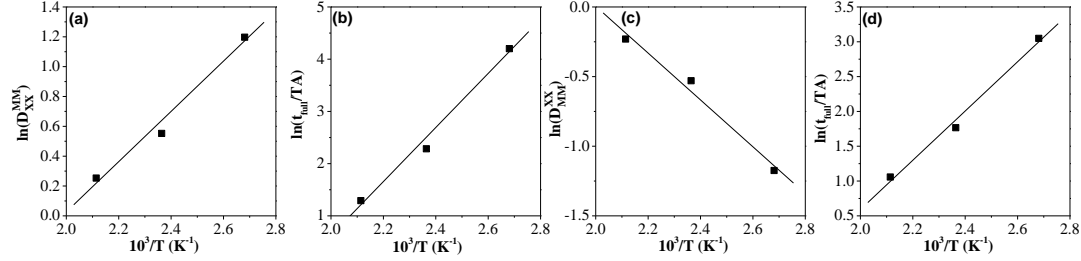


**Figure 6: (a)  $D_{XX}^{MM}$  vs.  $T$  based on Fig. 3(c)'s Region II. (b)  $t_{full}$  vs.  $T$  based on Fig. 3(d)'s Region II. (c)  $D_{MM}^{XX}$  vs.  $T$  based on Fig. 3(e)'s Region II. (d)  $t_{full}$  vs.  $T$  based on Fig. 3(f)'s Region II.**

#### 4.2. With surface energy

In the previous section, we neglected surface energy in our solution of Eqs. (4)-(5). A solution may be found which accounts for surface energy using the same numerical method discussed above. Surface energies from the work of Vitos [16] and Soon [17] were used without modification. The resulting normalized surface energy values are  $\gamma_a = 0.047$ ,  $\gamma_\rho = 0.0054$ , and  $\gamma_R = 0.020$  in the Cu/Cu<sub>2</sub>O system, where  $\gamma_a$  is the inner void surface energy,  $\gamma_\rho$  is the Cu/Cu<sub>2</sub>O interface energy, and  $\gamma_R$  is the outer Cu<sub>2</sub>O surface energy. The resulting contour plots show qualitatively similar trends, but with a solid/hollow phase boundary that is significantly shifted because surface energies increase the necessary initial driving force to develop a hollow structure. Fig. 7 shows contour plots which were developed by methods similar to Fig. 3 which include surface energy.



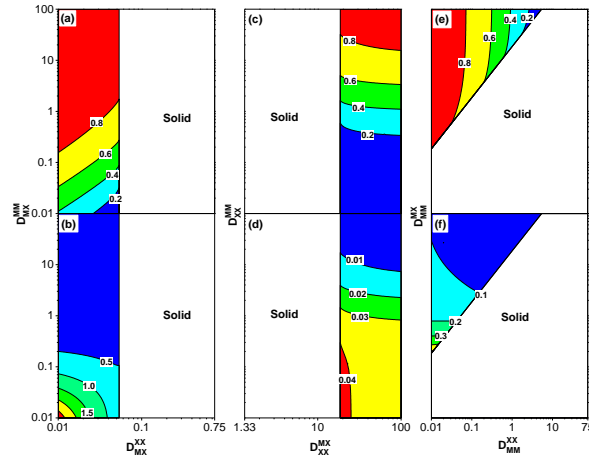


**Figure 7: Contour maps of  $a_f$  (a), (c), (e) and  $A$  (b), (d), (f) with surface energy. Oxidized NPs become hollow in  $D_{MX}^{XX} < 0.054$  and solid in  $D_{MX}^{XX} \geq 0.054$  for (a)-(b), hollow in  $D_{XX}^{MX} > 19$  and solid in  $D_{XX}^{MX} \leq 19$  for (c)-(d), hollow in  $D_{MM}^{XX} < 0.054 D_{MM}^{MX}$  and solid in  $D_{MM}^{XX} \geq 0.054 D_{MM}^{MX}$  for (e)-(f) when initial hollow radius  $a_0$  is taken as 0.066 which corresponds to one lattice constant with an initial particle radius of 5.5 nm.**

Analysis of the contour plots with surface energy reveals several rules for the formation of hollow nanoparticles. Mainly, including surface energy places a new requirement on the initial conditions for the system since  $a$  cannot have a value of zero in order for  $\dot{a}$  to be positive according to Eq. (4). In the initial stage of oxidation, that is  $a \sim 0$ ,  $\rho \sim R \sim 1$ ,  $\frac{v\Omega}{D_{MX}^{XX}} - (1 - u\Omega) - \frac{2\gamma_a\Omega}{a} \left[ \frac{(1-u\Omega)^2}{\Omega} + \frac{uv\Omega}{D_{MX}^{XX}} \right] > 0$  is the new criterion for  $\dot{a}$  to be positive in Eq. (4) and therefore for a hollow structure to form at all. This criterion requires that initial value of  $a$  should take a finite value which satisfies the condition of  $a_0 > \frac{2\gamma_a u \Omega (v\Omega + (1 - u\Omega)^2 D_{MX}^{XX} / u\Omega)}{(v\Omega - (1 - u\Omega) D_{MX}^{XX})}$ . As a result, we assume the smallest possible value of  $a_0$  which satisfies this criteria which is that of a single lattice constant of Cu. Specifically, we assume that  $a_0 = 0.066$  which corresponds to an actual initial void radius of 0.36 nm at an initial particle radius of 5.5 nm which corresponds to a single lattice vacancy in a face centered cubic Cu lattice [18].

Given this value of  $a_0$ , the new criteria for the formation of a hollow nanoparticle is  $(a_0 v \Omega - 2\gamma_a u v \Omega^2) / (a_0 (1 - u\Omega) + 2\gamma_a (1 - u\Omega)^2) > D_{MX}^{XX}$  which can be seen in Fig. 7 by the large shift in the solid/hollow phase boundary compared to Fig. 3. The solid/hollow boundary moves from  $D_{MX}^{XX} = 0.75$  without surface energy to  $D_{MX}^{XX} = 0.054$ . On the other hand, the overall behaviors of  $a_f$  and  $A$  in Fig. 7 on the hollow side of the phase boundary are qualitatively similar to those without surface energy in Fig. 3. The reason is that the surface energy term influences only the beginning of hollow void formation. Once  $a$  becomes large, the surface energy term becomes small due to the small magnitude of  $\gamma_a$ . Therefore the surface energy terms don't significantly influence  $a_f$  and  $A$  for the latter part of the reaction.

As a consequence of the large shift in the solid/hollow phase boundary, Fig. 7(e)-(f) shows that  $A$  is nearly constant in the experimentally measured  $a_f$  (0.65-0.50) region, which means that the full oxidation time is largely dependent only on  $D_{MM}$ . Therefore  $D_{MM}$  determines the time scale of

oxidation. In addition, in Fig. 7(e)  $a_f$  varies inversely with  $D_{MM}^{XX}$  and is almost independent of  $D_{MM}^{MX}$ , which means that the ratio of oxygen diffusivity in the metal oxide phase,  $D_{XX}$  to the metal's diffusivity in the metal phase,  $D_{MM}$  is the only contributing factor to the size of the hollow void and that  $D_{MX}$  doesn't influence the kinetics of the system much because  $D_{MX}$  is larger than  $D_{MM}$ . This is in contrast to the conventional understanding of the nanoscale Kirkendall effect, which implies that the void size is only dependent on the ratio of the two diffusivities in the binary phase [1].

Using Fig. 7 along with experimentally measured hollow radii shows that in this system,  $D_{MX}^{MM}$  must be less than 0.40 since the largest measured radii was 0.65 and the largest value of  $D_{MX}^{MM}$  in Fig. 7(a) corresponding to  $a_f = 0.65$  is 0.40. This is a critical finding because previous work operated under the assumption that  $D_{MM}$  is much larger than  $D_{MX}$  due to hydrostatic tensile stresses during oxidation [12]. In this case however, we have shown just the opposite; that  $D_{MM}$  may never be larger than  $D_{MX}$  in order for hollow structures to form. Therefore the previous assumption overestimates the effect on diffusivity of hydrostatic tensile stresses by at least two orders of magnitude.

The inclusion of surface energy also improves the ability of this model to extract diffusion parameters. Since the solid/hollow boundary shifts to the left in Fig. 7(a)-(b) due to the inclusion of surface energy, Region I from section 4.1.1 no longer exists, so the assumption of a large  $D_{MX}^{MM}$  value is no longer plausible. On the other hand Fig. 7(c) shows that  $D_{MX}^{MM}$  is nearly constant over the entire region of experimentally measured values for  $a_f$  (0.65-0.50) due to the move of the solid/hollow boundary from  $D_{XX}^{MX} = 4/3$  to  $D_{XX}^{MX} = 19$ . Using methods similar to those shown above for Region II, Fig. 7(d) shows that  $A$  is nearly constant along each  $a_f$  line. Therefore we can extract approximate values of  $D_{XX}^{MX}$  for each temperature using the same methodology as with Region II above. Assuming  $D_{XX}^{MX} = 100$ ,  $D_{XX}^{MM}$  is equal to 4.6 at 100°C, 2.5 at 150°C, and 1.9 at 200°C. Applying these values to Fig. 7(d),  $A$  is equal to 0.014 at 100°C, 0.019 at 150°C, and 0.022 at 200°C. Combining all of the above data and fitting it by least squares fitting to a linearized plot in Fig. 8(a)-(b), leads to:

$$D_{XX}^{MM} = D_{OinCu_2O}^{CuinCu} = 0.068 \exp(13/R_g T) \quad (15)$$

$$D_{XX} = D_{OinCu_2O} = 90 \exp(-43/R_g T) \text{ (nm}^2/\text{s)} \quad (16)$$

$$D_{MM} = D_{CuinCu} = 6.1 \exp(-30/R_g T) \text{ (nm}^2/\text{s)} \quad (17)$$

Surprisingly, the resulting diffusivities are similar to those found without surface energy in section 4.1.2 because of qualitatively similar trends of contour plots as discussed above. On the other hand, the values found using surface energy terms are considerably more useful because they do not require any assumption about the relative values of  $D_{MX}$  and  $D_{MM}$  or  $D_{XX}$ .

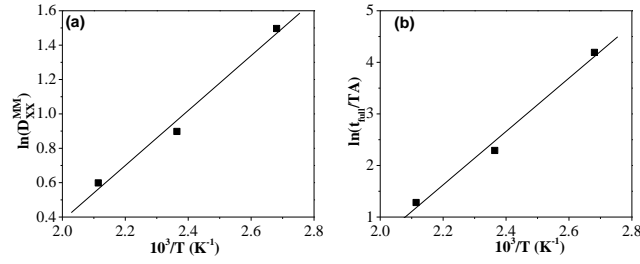


Figure 8: (a)  $D_{XX}^{MM}$  vs.  $T$  based on Fig. 7(c). (b)  $t_{full}$  vs.  $T$  based on Fig. 7(d).

#### 4.3. Comparison to literature

Comparing our results to values of bulk Cu and  $Cu_2O$  from the literature, we find large discrepancies in the values of  $D_{CuinCu}$  and  $D_{OinCu_2O}$  which have previously been found to be  $D_{CuinCu} = 2.0 * 10^{13} \exp(-197/R_g T) (nm^2/s)$  [19] and  $D_{OinCu_2O} = 3 * 10^{11} \exp(-150/R_g T) (nm^2/s)$  [20]. This is not surprising as it is consistent with previous findings that  $D_{CuinCu}$  in a Cu/ $Cu_2O$  nanoparticle system is increased by 6-11 orders of magnitude. Therefore it is still necessary to account for the increase in  $D_{CuinCu}$  by hydrostatic tensile stresses at the Cu/ $Cu_2O$  interface during oxidation [12]. In addition, our calculated value of  $D_{OinCu_2O}$  is 2-5 orders of magnitude larger than the extrapolated literature value. This enlarged diffusivity may be attributed to the influence of grain boundary diffusion in our experimental data.

Finally, the value for  $D_{CuinCu_2O}$  has been previously found to be  $D_{CuinCu_2O} = 3.7 * 10^{10} \exp(-102/R_g T) + 4.1 * 10^{13} \exp(-170/R_g T) (nm^2/s)$  [21] which combined with the calculated value for  $D_{OinCu_2O}$  results in a value of  $D_{XX}^{MX} = D_{OinCu_2O}^{CuinCu_2O} \leq 19$  at  $100^\circ C$ . This value should result in a solid nanoparticle, but if  $D_{CuinCu_2O}$  is increased in the same manner as the other diffusivities, then it is reasonable to conclude that  $D_{CuinCu} \ll D_{CuinCu_2O}$  in our nanoparticle system.

## 5. Conclusion

Based on a combination of experimental data and an expansion upon the model originally developed by Svoboda et al., we extracted the diffusivity parameters  $D_{CuinCu}$  and  $D_{OinCu_2O}$  for the oxidation of a Cu nanoparticle. We found that the addition of surface energy in the kinetic model induces a shift of the solid/hollow phase boundary towards larger values of  $D_{CuinCu_2O}$  compared to  $D_{OinCu_2O}$ . This shift allowed for the extraction of  $D_{CuinCu}$  and  $D_{OinCu_2O}$  without any prior assumptions about the relative magnitudes of  $D_{CuinCu}$  and  $D_{CuinCu_2O}$ , revealed the specific role of each of the three characteristic diffusivities:  $D_{CuinCu}$  determines the time scale of oxidation, the ratio of values of  $D_{OinCu_2O}$  and  $D_{CuinCu}$  determines the void size, and  $D_{CuinCu_2O}$  is largely irrelevant in the kinetics of oxidation.

## References

- [1] Yin Y, Rioux RM, Erdonmez CK, Hughes S, Somorjai GA, Alivisatos AP. *Science* 2004;304:711.
- [2] Nakamura R, Tokozakura D, Nakajima H, Lee J-G, Mori H. *J Appl Phys* 2007;101:074303.
- [3] Tokozakura D, Nakamura R, Nakajima H, Lee J-G, Mori H. *J Mater Res* 2007;22:2930.
- [4] Nakamura R, Lee J-G, Mori H, Nakajima H. *Phil Mag* 2008;88:257.
- [5] Yin Y, Erdonmez CK, Cabot A, Hughes S, Alivisatos AP. *Adv Funct Mater* 2006;16:1389.
- [6] Wang CM, Baer DR, Thomas LE, Amonette JE, Antony J, Qiang Y, Duscher G. *J Appl Phys* 2005;98:094308.
- [7] Nakamura R, Lee J-G, Tokozakura D, Mori H, Nakajima H. *Mater Lett* 2007;62:1060.
- [8] Cho HJ, Hwang PG, Jung D. *J Phys Chem Solids* 2011;72:1462.
- [9] Zhou XW, Gan YL, Sun SG. *Acta Phys-Chim Sin* 2012;28:2071.
- [10] Hu SH, Chen SY, Liu DM, Hsiao CS. *Adv Mater* 2008;20:2690.
- [11] Luo B, Xu SA, Ma WF, Wang WR, Wang SL, Guo J, Yang WL, Hu JH, Wang CC. *J Mater Chem* 2010;20:7107.
- [12] Svoboda J, Fischer FD, Vollath D. *Acta Mater* 2009;57:1912.
- [13] Svoboda J, Turek I, Fischer FD. *Phil Mag* 2005;85:3699.
- [14] Rice K, Paterson A, Stoykovich M. *Submitted*
- [15] Yin M, Wu CK, Lou YB, Burda C, Koberstein JT, Zhu YM, O'Brien SJ. *Am Chem Soc* 2005;127:9506.
- [16] Vitos L, Ruban A, Skriver H, Kollar J *Surf Sci* 1998;411:186
- [17] Soon A, Todorova M, Delley B, Stampfl C. *Phys Rev B* 2007;75:125420; 2007;76:129902
- [18] Clark SP Jr., editor. *Handbook of physical constants*. New Haven: The Geological Society of America, Yale University; 1966.
- [19] Neumann G, Tuijn C. *Self-diffusion and impurity diffusion in pure metals: handbook of experimental data*. Amsterdam: Pergamon; 2009
- [20] Perinet F, Barbezat S, Monty C. *J de Phys* 1980;C6:315
- [21] Peterson NL, Wiley CL. *J Phys Chem Solids* 1984;45:281

# Chapter III - Intermediate Morphology of Cu/Cu<sub>2</sub>O Nanoparticles during Reduction by H<sub>2</sub> as determined by in-situ UV-Vis spectroscopy

## Introduction

Cu and Cu<sub>2</sub>O catalysts have been shown to greatly improve their activity for a variety of reactions following “activation” by using small amounts of O<sub>2</sub> or H<sub>2</sub> to create surface structures that are not entirely composed of one phase or the other, but have characteristics of both at the surface [1]. For the water gas shift (WGS) reaction, Cu catalysts are used in the presence of 2% oxygen in order to improve their selectivity and reactivity [1]. This effect was explained by the fact that the lowest surface energy sites on Cu<sub>2</sub>O under 2% O<sub>2</sub> were non-stoichiometric or partially reduced surface structures. Having shown that the intermediate structures between Cu and Cu<sub>2</sub>O in nanoparticles systems are particularly important for practical applications, it is then necessary to fully characterize the reduction and oxidation process which alters the system between the two states in order to fully optimize the Cu/Cu<sub>2</sub>O system.

Others have previously addressed this topic from a kinetic angle using in-situ XRD and TGA/d-TGA measurements for CuO and Cu<sub>2</sub>O, but the overall mechanism for reduction isn't fully characterized because traditional kinetic measurements give time resolved mass loss or phase change data that can be fit to a variety of models, but do not give insight into intermediate structures or the morphology of the particles during reduction [2-5]. On the other hand, In-situ UV-Vis characterization combined with simple Mie scattering calculations can provide a way to infer intermediate structures and confirm the previous measurements performed by other methods.

There are two possible mechanisms for the reaction of hydrogen gas with metal oxide: the reaction could occur between adsorbed hydrogen and lattice oxygen at the surface followed by desorption of the H<sub>2</sub>O product or the reaction could occur between hydrogen embedded in the lattice and subsurface oxygen followed by the outward diffusion of the H<sub>2</sub>O product. Given the energetic penalty for the diffusion of hydrogen into the lattice combined with the formation of H<sub>2</sub>O within the lattice and its outward diffusion, the surface reaction scenario is highly favored [4, 6, 7].

In considering the intermediate structures of partially reduced metal oxide nanoparticles it is wise to start with the accepted mechanisms for reduction in the bulk phase. Two different mechanisms have been proposed in the literature for the reduction of bulk transition metal oxide surfaces by hydrogen which may be applied to nanoparticle reduction: the interface controlled model and the nucleation model ([7, 8]). In the interface controlled model, the entire surface of the metal oxide is reduced evenly and a metal/oxide interface advances into the substrate uniformly. In the nucleation model, islands of reduced oxide form on the surface and advance into the substrate isotropically until they come into contact with neighboring islands. From that point the reduced oxide surface advances into the substrate in a similar fashion to the advancing metal interface model. For long reaction times both

models converge on the same situation in which lattice oxygen must diffuse through a metal or reduced oxide layer in order for the reaction to continue, creating a self-limiting situation.

With this in mind, the nanoparticle reduction mechanism may be qualitatively different from the bulk surface reduction mechanism because the maximum diffusion length for lattice oxygen to reach the surface from the center of a nanoparticle is considerably shorter than for the bulk. In fact, if the diffusion length is small enough and the diffusivity of oxygen vacancies in the oxide phase is fast enough a metal core may form in the center of the nanoparticle due to an aggregation of oxygen vacancies. In this work, we propose that the mechanism for the reduction of  $\text{Cu}_2\text{O}$  nanoparticles by hydrogen gas follows a nucleation mechanism on the surface combined with an aggregation of oxygen vacancies in the center of the particle which forms a metal core. The evidence for this proposed mechanism is shown by in-situ UV-Vis characterization combined with UV-Vis modeling for the various proposed intermediate structures associated with the reduction process.

## Materials and Methods

All chemicals were purchased from Sigma-Aldrich and used as received. Colloidal copper nanocrystals were synthesized by reduction of copper precursors in solution as previously reported by Yin et al[9]. The nanocrystals were then washed in ethanol and redispersed in hexane which was then deposited on clean glass slides to form nanoparticle films. The films were then oxidized in ambient atmosphere on a hotplate at 200C for 30 minutes to form  $\text{Cu}_2\text{O}$ .

Oxidized nanoparticle films were then placed in a heated flow reactor under .2 liters per minute of ultra-high purity  $\text{H}_2$  at 135-190C and monitored via UV-Vis throughout the duration of the experiment using an Ocean Optics USB4000 spectrometer. The reaction was stopped when the UV-Vis spectra reached steady state.

Peak height and wavelength for each spectrum was compiled by fitting the absorption spectra between 450 and 850 nm to a double exponential plus sixth order polynomial function and extracting the peak height and wavelength from the fitted curve.

Mie scattering calculations were performed using software developed by Pena et al [10] using the dielectric functions taken from ref [11] and adjusted for size as demonstrated elsewhere[12]. The dielectric constant of the medium was taken to be the same as the capping ligand oleic acid ( $\epsilon=2.4$ ).

## Results and Discussion

### Intermediate Structure Results:

Our data is consistent with the nucleation mechanism in which the islands of reduced copper at the surface grow as adsorbed hydrogen reacts with surface oxide species. When surface oxygen species are removed by hydrogen, oxygen vacancies are created. Combined with the positively charged adsorbed hydrogen these vacancies create a driving force for lattice oxygen to diffuse to the surface, which leaves

a growing number of oxygen vacancies throughout the lattice. Outward diffusing oxygen encourages these vacancies to aggregate and form a reduced copper core.

As a visual aid, one can picture this structure as a three-layered sphere as shown in Figure 1. The inside layer is copper, the intermediate layer is  $\text{Cu}_2\text{O}$ , and the outer layer is a mix of Cu islands and  $\text{Cu}_2\text{O}$ . The outermost layer maintains an assumed constant thickness throughout the reaction of 4 Å (one monolayer) and reaches a pseudo-steady-state area fraction of copper islands as surface oxygen removal balances with outward oxygen diffusion from the lattice.

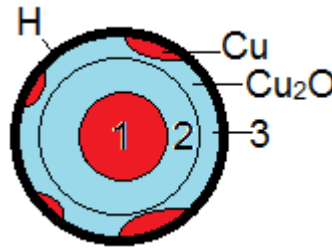


**Figure 1: A three layered model for predicting the optical response of the intermediate structure of  $\text{Cu}_2\text{O}$  undergoing reduction by  $\text{H}_2$ . The outermost layer is composed of islands of Cu in a layer of  $\text{Cu}_2\text{O}$ . The middle and core layer are composed of  $\text{Cu}_2\text{O}$  and Cu respectively.**

In order to predict the optical response of this intermediate structure, a 3-layered model was analyzed using Mie scattering and effective medium theory. The inputs to this model are (1) a size factor for each layer which is proportional to the layer's radius, (2) a dielectric function for each layer. In this model the core layer is Cu, the intermediate layer is  $\text{Cu}_2\text{O}$ , and the surface layer is a mix of Cu and  $\text{Cu}_2\text{O}$  with an area fraction of 75% Cu as shown in Figure 1. The surface layer dielectric was predicted by assuming that the surface layer was 75% Cu and 25%  $\text{Cu}_2\text{O}$  in a random arrangement in which the layers were perpendicular to the applied electric field. The resulting equation for the surface layer dielectric function is shown as equation 1[13].

$$\epsilon_{eff}^{-1} = f_{Cu}\epsilon_{Cu}^{-1} + f_{Cu_2O}\epsilon_{Cu_2O}^{-1} \quad \text{Eq. 1}$$

The effective dielectric function of the surface layer is then calculated using the size-corrected dielectric function of Cu[11, 12], the dielectric function of  $\text{Cu}_2\text{O}$ [11], and the area fractions of both phases on the surface.

Figure 2 shows the result of the Mie scattering calculations. This raw data does not directly fit with the observed experimental spectra for small core sizes due to the red-shifted peaks, but for larger core sizes it fits very well.

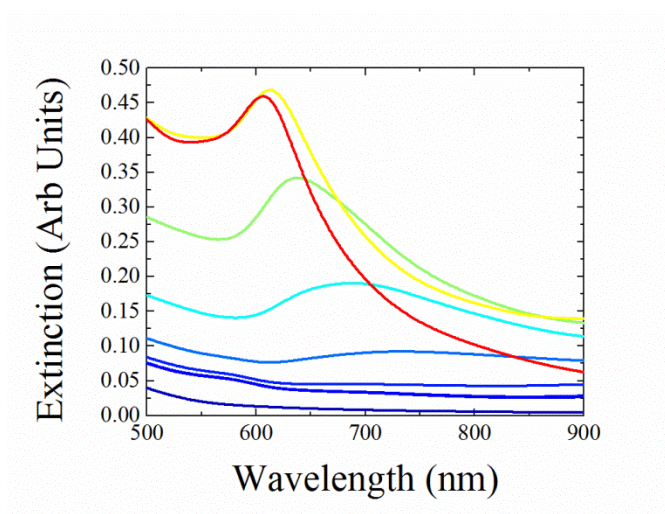


**Figure 2: Raw Mie scattering spectra from Cu<sub>2</sub>O (blue) to fully reduced Cu (red). Intermediate spectra correspond to various Cu core diameters.**

The induction period associated with the reduction of transition metal oxides is likely to be a stochastic process [7](also cite transition metal oxides book). As a result, it is expected that at any given point in time an ensemble of particles undergoing reduction has a non-homogenous distribution of core diameters. The optical response associated with this ensemble of particles must then be comprised of a linear combination of many different particle spectra which are weighted based on the density of particles with a particular core diameter. To model this distribution of core sizes we assumed a distribution of induction times with a mean of 50 minutes and a standard deviation of 20 minutes, which is derived from the observed induction time of approximately 10 minutes (at 150C) with the assumption that we would observe the first change in optical spectra when about 10% of the particles finish the induction period. Using this distribution of induction times in conjunction with the kinetic model discussed below, a distribution of core radii vs. time was developed and combined with the raw Mie scattering spectra to create a predicted optical spectrum for each time point as shown in Figure 3. For short times the model fails to accurately reproduce the experimental peak wavelength and height. At intermediate and long times, however, the behavior of the model is very similar to experimental results.



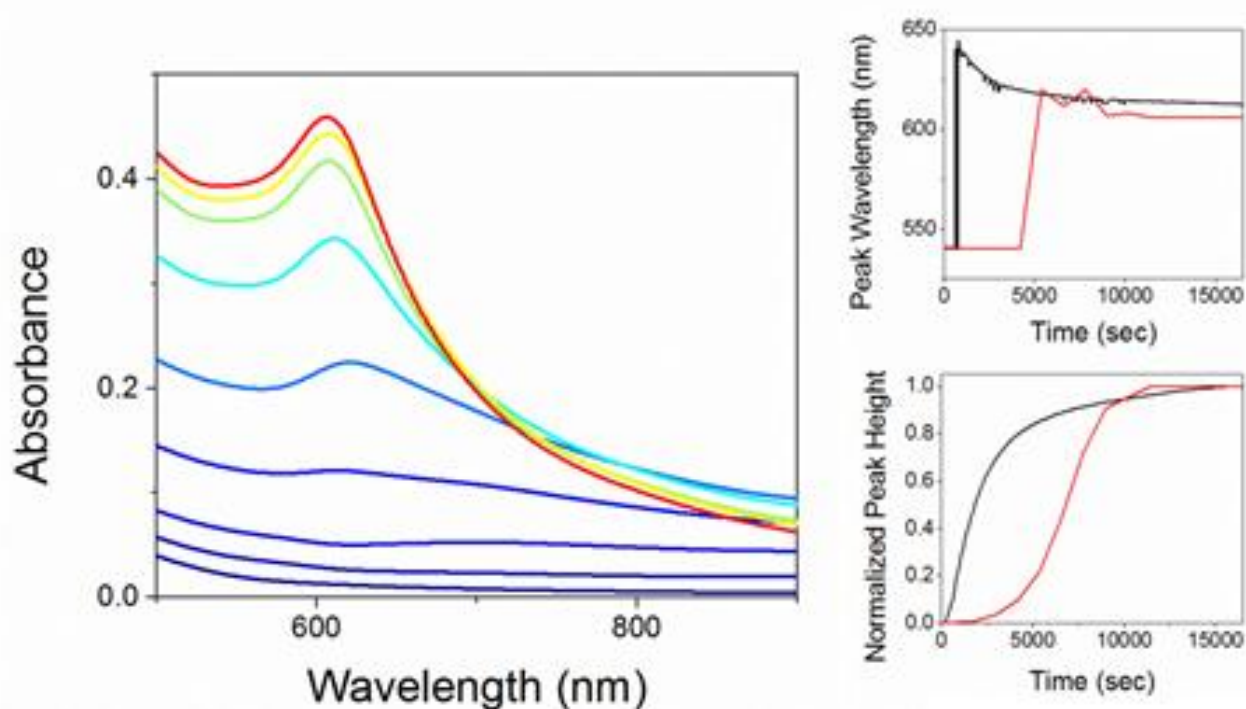


Figure 3: (a) Predicted UV-Vis spectra. (b) Experimental and model peak wavelength vs time. (c) Experimental and model peak height vs time.

Using the same methods described above, Mie scattering was used to predict the UV-Vis spectra of Cu nanoshells with Cu<sub>2</sub>O core consistent with the interface controlled mechanism. Figure 4 shows the predicted spectra for Cu nanoshells with .5, 1, and 1.5 nm shell thicknesses. The thin shelled spectra show very strong absorbance in the near-IR (~850 nm) which blue-shifts as the shell thickness increases. This data suggests that Cu<sub>2</sub>O nanoparticle reduction does not occur via the interface controlled mechanism because the predicted spectra are inconsistent with experimentally observed spectra which show the first peak around 650 nm and only slightly blue shifts to 620 nm after full reduction. No linear combination of nanoshell spectra could reproduce the experimentally observed spectra due to the strong absorption of thin nanoshells at near-IR wavelengths.

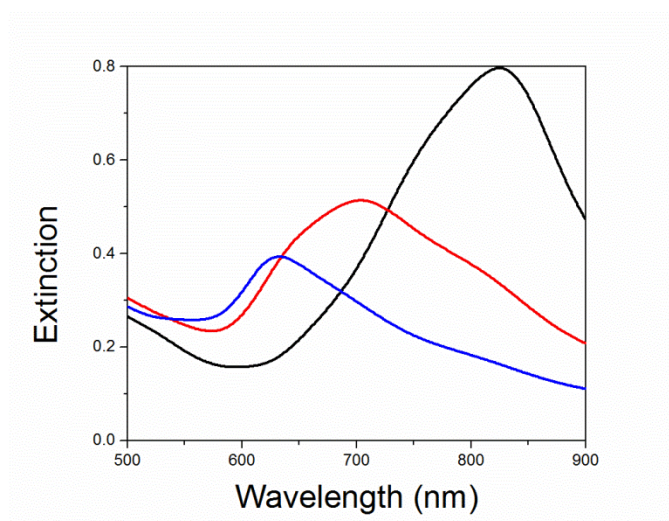


Figure 4: Predicted spectra for Cu<sub>2</sub>O core Cu shell nanoparticle. Shell thicknesses are .5nm (black), 1 nm (red), and 1.5nm (blue).

#### Kinetic Results:

By analyzing our in-situ UV-Vis data to extract plasmon peak wavelength and height as a function of time, we are able to extract kinetic parameters which are important for practical applications of Cu/Cu<sub>2</sub>O systems. In particular, we tracked the plasmon peak height and correlated it to extent of reduction and found time for full reduction associated with each temperature as shown in Figure 5. This plot was used with a theoretical model to extract diffusivity parameters  $E_d$  and  $D_0$  which are the activation energy and diffusion constant for oxygen in Cu<sub>2</sub>O.

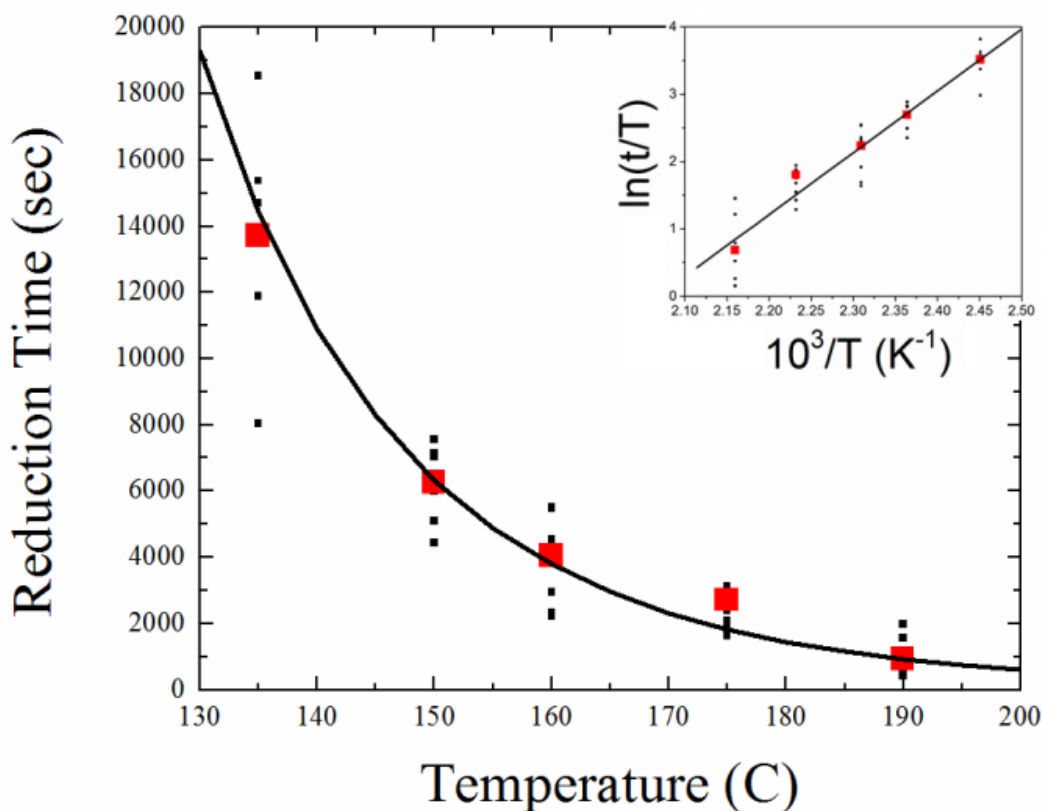
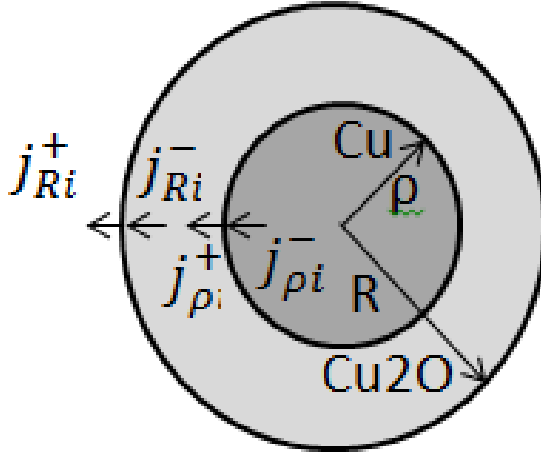


Figure 5: Average reduction time vs. Temperature for all trials. Averages (red squares) fit the expression for reduction time at a given temperature developed below (black line). The inset shows the linearized plot which was used to find the diffusivity of oxygen in  $\text{Cu}_2\text{O}$ .

The nucleation reduction mechanism proposed above can be modeled in a similar fashion to Cu NP oxidation as previously demonstrated by Svoboda et al[14]. Using the same basic methodology, reduction is modeled with a different starting geometry and assuming a surface reaction instead of a reaction at the oxide/metal interface. In this model, the nanoparticle is assumed to be spherical with a Cu core and  $\text{Cu}_2\text{O}$  shell (See Fig. 6). Another key difference is that this model tracks the development of the core radius,  $\rho$ , by following the outward diffusion of oxygen through the  $\text{Cu}_2\text{O}$  phase. Finally, this model assumes the particle to be solid in contrast to ref 5 which tracks the development of a hollow core through the oxidation process. By oxidizing Cu at higher temperatures during our sample preparation, we ensure that our starting material has collapsed to a solid core.



**Figure 6: Assumed particle geometry for the diffusion model. The core phase is Cu and the outer phase is Cu<sub>2</sub>O. The variables at each interface indicate the net flux of component i across boundary  $\rho$  and R. For the purposes of this model, the surface nucleation sites are assumed to have a negligible effect on the diffusion characteristics of the system.**

Following the same derivation as shown by Svoboda et al[14], the kinetics of this system are given by the following equation which is derived from the thermodynamic extremal principle[15] with copper core radius  $\rho$  being the independent variable.

$$\frac{1}{2} \frac{\partial^2 Q}{\partial \rho^2} \dot{\rho} = - \frac{\partial \dot{G}}{\partial \rho} \quad \text{Eq 2}$$

Here  $Q$  and  $G$  are the energy dissipation function and the Gibbs free energy of the system, respectively, which vary according to equations 3 and 4. In order to simplify the derivation, strain energy is neglected as in[14]. Here  $R_g$  is the gas constant,  $T$  is temperature,  $v$  is the molar ratio of O in Cu<sub>2</sub>O,  $\Omega_{\text{Cu}_2\text{O}}$  and  $\Omega_{\text{Cu}}$  are the molar volume of Cu<sub>2</sub>O and Cu respectively,  $D_{\text{O in Cu}_2\text{O}}$  and  $D_{\text{Cu in Cu}_2\text{O}}$  are the diffusivities of O and Cu in Cu<sub>2</sub>O,  $\Delta g_{\text{Cu}}$  is the change in gibbs free energy for reduction of Cu<sub>2</sub>O by H<sub>2</sub>, and  $\gamma_\rho$  and  $\gamma_R$  are the surface energies at the interfaces  $\rho$  and R respectively.

$$Q = \frac{4\pi R_g T v \rho^4 \dot{\rho}^2}{\Omega_{\text{Cu}_2\text{O}} D_{\text{O in Cu}_2\text{O}}} \left( \frac{1}{\rho} - \frac{1}{R} \right) + \frac{4\pi \Omega_{\text{Cu}_2\text{O}} R_g T \rho^4 \dot{\rho}^2}{u D_{\text{Cu in Cu}_2\text{O}}} \left( \frac{1}{\Omega_{\text{Cu}}} - \frac{u}{\Omega_{\text{Cu}_2\text{O}}} \right)^2 \left( \frac{1}{\rho} - \frac{1}{R} \right) \quad \text{Eq 3}$$

$$G = G_0 + \frac{4\pi}{3} \rho^3 \frac{\Delta g_{\text{Cu}}}{\Omega_{\text{Cu}}} + 4\pi \gamma_\rho \rho^2 + 4\pi \gamma_R (R^2 - R_0^2) \quad \text{Eq 4}$$

In order to simplify the analysis, non-dimensional quantities for time, diffusivity, radius, and surface energy are introduced in equations 5-10, which are slightly modified from ref [14] to fit the reduction mechanism. In particular, the diffusivity of Cu in Cu<sub>2</sub>O is replaced with the diffusivity of O in Cu<sub>2</sub>O because this model deals with O as the diffusing species. In addition, a relationship is developed

between the outer radius  $R$  and core radius  $\rho$  by the conservation of Cu in the system as Eq. 12 in order to write the system equations in terms of a single independent variable.

$$\tau = \frac{R_g T R_o^2}{D_{OinCu2O} |\Delta g_{Cu}|} \quad \text{Eq 5}$$

$$\bar{t} = \frac{t}{\tau} \quad \text{Eq 6}$$

$$D_{M/X} = D_{CuinCu2O} / D_{OinCu2O} \quad \text{Eq 7}$$

$$\bar{\rho} = \frac{\rho}{R_o} \quad \text{Eq 8}$$

$$\bar{\gamma}_\rho = \frac{\gamma_\rho \Omega_{Cu2O}}{|\Delta g_{Cu}| R_o} \quad \text{Eq 9}$$

$$\bar{\gamma}_R = \frac{\gamma_R \Omega_{Cu2O}}{|\Delta g_{Cu}| R_o} \quad \text{Eq 10}$$

$$\Omega = \frac{\Omega_{Cu}}{\Omega_{Cu2O}} \quad \text{Eq 11}$$

$$\bar{R} = \left( 1 - \frac{1-u\Omega}{u\Omega} \bar{\rho}^3 \right)^{\frac{1}{3}} \quad \text{Eq 12}$$

Then Eq. 2 is rewritten in normalized quantities as Eq 13.

$$\left( \frac{(1-u\Omega)^2}{u\Omega D_{M/X}} + v\Omega \right) \frac{\bar{R}-\bar{\rho}}{\bar{R}} \bar{\rho} \frac{d\bar{\rho}}{d\bar{t}} = 1 - \frac{2\bar{\gamma}_\rho \Omega}{\bar{\rho}} + \frac{2\bar{\gamma}_R \Omega}{\bar{R}} \frac{(1-u\Omega)}{\Omega} \quad \text{Eq 13}$$

In order to simplify the derivation to end up with a useful solution, we assumed that the surface energies  $\bar{\gamma}_\rho$  and  $\bar{\gamma}_R$  are negligible. To justify this assumption, we assume values of surface energy from the literature to calculate  $\bar{\gamma}_\rho$  and  $\bar{\gamma}_R$ . If we take

$\gamma_R = 7.85 * 10^{-22} \text{ kJ/nm}^2$  Error! Bookmark not defined. and

$\gamma_{Cu} = 1.8 * 10^{-21} \text{ kJ/nm}^2$  Error! Bookmark not defined., then  $\bar{\gamma}_\rho = 4.50 * 10^{-3}$ , and  $\bar{\gamma}_R = 1.05 * 10^{-2}$ , both of which are much less than 1. Therefore the assumption to neglect surface energy is justified because for reasonable values of  $\bar{\gamma}_\rho$  and  $\bar{\gamma}_R$ , the right side of Eq 9 is very close to 1.

With surface energy neglected, Eq. 13 can be integrated as Eq 14.

$$\left( \frac{(1-u\Omega)^2}{u\Omega D_{M/X}} + v\Omega \right) \left( \frac{\bar{\rho}^2}{2} + \frac{u\Omega}{2(1-u\Omega)} \left[ \left( 1 - \frac{(1-u\Omega)}{u\Omega} \bar{\rho}^3 \right)^{\frac{2}{3}} - 1 \right] \right) = \bar{t} \quad \text{Eq 14}$$

Because of the  $\frac{(1-u\Omega)^2}{u\Omega D_{M/X}}$  term in Eq. 14 the behavior of the system is largely dependent on the relative diffusivity of the two species in the oxide layer. In this case since the diffusivity of Cu in Cu<sub>2</sub>O is several orders of magnitude larger than the diffusivity of O in Cu<sub>2</sub>O for the temperature ranges explored in this study[16-18], we can assume  $D_{M/X} \gg 1$ , and the  $\frac{(1-u\Omega)^2}{u\Omega D_{M/X}}$  is negligible. Under this assumption Eq. 14 becomes:

$$\bar{t} = v\Omega \left( \frac{\bar{\rho}^2}{2} + \frac{u\Omega}{2(1-u\Omega)} \left[ \left( 1 - \frac{(1-u\Omega)}{u\Omega} \bar{\rho}^3 \right)^{\frac{2}{3}} - 1 \right] \right) \text{ Eq 15}$$

Eq. 15 is plotted as  $\bar{\rho}$  vs.  $\bar{t}$  in Fig. 7. In the beginning (small  $\rho$  region) the Cu core increases rapidly as  $\bar{\rho} \approx \sqrt{\bar{t}}$  because when  $\rho$  is small,  $\dot{\rho}$  must be large in order to dissipate the change in Gibbs free energy created by the formation of the Cu phase. Near the end when  $\rho \approx R$ , the Cu core increases rapidly as  $|\bar{\rho} - \bar{\rho}_f| \approx \sqrt{|\bar{t} - \bar{t}_f|}$  because of the short diffusion path from  $\rho$  to  $R$ .

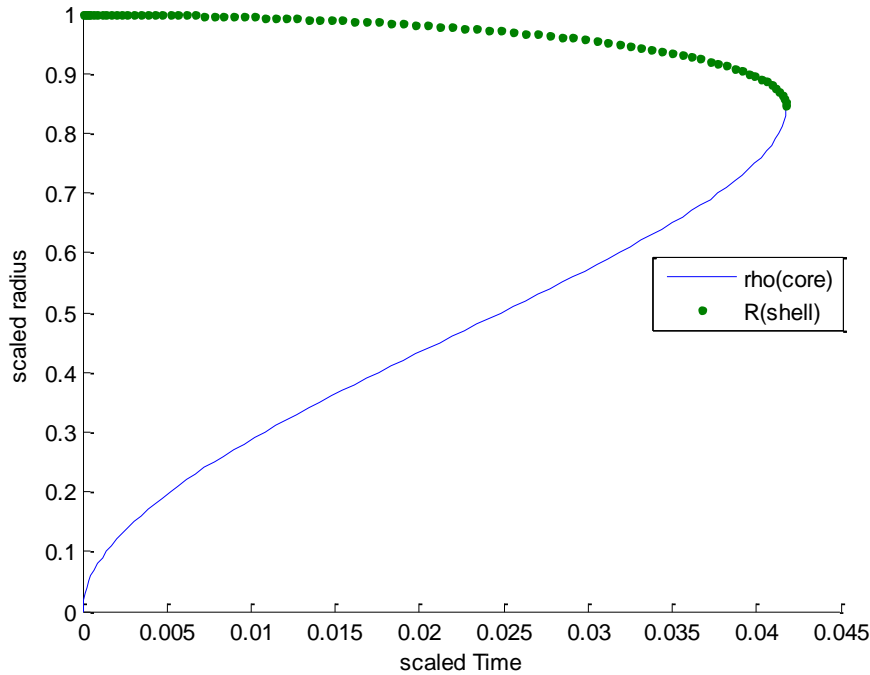


**Figure 7: Model plot of non-dimensional core-radius vs non-dimensional time.**

In order to fit our experimental data to the model, we collected times of full reduction by extracting normalized peak height vs. time for all trials at temperatures of 135, 150, 160, 175, and 190C. Time of

full reduction,  $t_{full}$ , was taken as the time for normalized peak absorbance to reach .95. Diffusivity of oxygen in  $Cu_2O$  takes the form of Eq 16, where  $E_d$  is the diffusion energy and  $D_0$  is the diffusivity constant.

$$D_{OinCu_2O} = D_0 \exp(-E_d/R_g T) \quad \text{Eq 16}$$

Modifying Eq 15 to apply only to full reduction time where  $\bar{\rho} = (u\Omega)^{1/3}$  and substituting in dimensional time leads to Eq 17.

$$t_{full} = \frac{R_g T R_0^2 v \Omega}{D_0 e^{\frac{-E_d}{R_g T}} |\Delta g_{Cu}|} \left( \frac{(u\Omega)^{2/3} - u\Omega}{2(1-u\Omega)} \right) \quad \text{Eq 18}$$

The resulting equation shows that  $t_{full}$  is only a function of the diffusivity constant and temperature. In order to make data fitting more practical to this model, we linearized Eq 17 to Eq 18 in which plotting  $\ln(t_{full}/T)$  vs  $1/T$  is a linear function as shown in the inset of Figure 5.

$$\ln\left(\frac{t_{full}}{T}\right) = \frac{E_d}{R_g} \frac{1}{T} + \ln\left(\frac{R_g R_0^2 v \Omega}{D_0 |\Delta g_{Cu}|} \left( \frac{(u\Omega)^{2/3} - u\Omega}{2(1-u\Omega)} \right)\right) \quad \text{Eq 18}$$

The resulting value of  $D_0$  is  $5.1 * 10^{-10} \text{ cm}^2/\text{s}$  and  $E_d$  is 76.3 kJ/mol. The value for self-diffusivity of oxygen in  $Cu_2O$  was found to be  $D_0 = 3 * 10^{-3} \text{ cm}^2/\text{s}$  and  $E_d = 150 \text{ kJ/mol}$  [16] by tracer diffusion methods. Our experimental  $D_0$  is considerably smaller than the self-diffusion value and  $E_d$  is about half of the self-diffusion value. The resulting value for the diffusivity of oxygen in cuprous oxide at the temperatures investigated in this study is two orders of magnitude larger than the extrapolated diffusivity that would be expected from the reported tracer self-diffusion values. The much faster diffusion observed in this study may be attributed to grain boundary diffusion which is likely a large factor in these nanoparticles which had undergone oxidation immediately before reduction which leads to polycrystalline structures. In addition, the adsorbed hydrogen at the surface of the particle could be contributing to faster diffusion by creating an electrostatic driving force for the diffusion of the negatively charged oxygen ions in the lattice.

## Conclusion

The intermediate structure of  $Cu/Cu_2O$  nanoparticles during reduction by hydrogen gas at various temperatures was investigated by in-situ UV-Vis spectroscopy. It was determined that the reduction process proceeds through an island growth mechanism with the outward diffusion of oxygen through the oxide phase causing an aggregation of vacancies which creates a metal core. By applying a previously developed kinetic model for the reaction of a biphasic metal sphere to reduction, the diffusivity parameter  $D_{OinCu_2O}$  was calculated as  $5.1 * 10^{-10} * \exp(76.3/R_g T) \text{ cm}^2/\text{s}$ , which is larger than

extrapolated literature values, but reasonable considering the difference between tracer diffusion and diffusion during reduction. The methodology employed in this study did not produce a good fit for the optical spectra at the beginning of the reduction process, but was consistent with the latter half. This disagreement is likely due to the fact that this model does not account for particle-particle interactions, slight polydispersity of our synthesized nanoparticles, and potential structural changes that occur to Cu<sub>2</sub>O nanoparticles at high temperatures.

## References

- [1] Soon A, Todorova M, Delley B, Stampfl C. Surface oxides of the oxygen-copper system: Precursors to the bulk oxide phase? *Surface Science* 2007;601:5809.
- [2] Pike J, Chan S-W, Zhang F, Wang Z, Hanson J. Formation of stable Cu<sub>2</sub>O from reduction of CuO nanoparticles. *Applied Catalysis A: General* 2006;303:273.
- [3] Goldstein EA, Mitchell RE. Chemical kinetics of copper oxide reduction with carbon monoxide. *Proceedings of the Combustion Institute* 2010.
- [4] Kim JY, Rodriguez JA, Hanson JC, Frenkel AI, Lee PL. Reduction of CuO and Cu<sub>2</sub>O with H<sub>2</sub>: H Embedding and Kinetic Effects in the Formation of Suboxides. *Journal of the American Chemical Society* 2003;125:10684.
- [5] Rodriguez JA, Kim JY, Hanson JC, Perez M, Frenkel AI. Reduction of CuO in H<sub>2</sub>: in situ time-resolved XRD studies. *Catalysis Letters* 2002;85:247.
- [6] Schollz JJ, Langell MA. Kinetic Analysis of Surface Reduction in Metal Oxide Single Crystals. *Surface Science* 1985;164:534.
- [7] Rodriguez JA, Hanson JC, Frenkel AI, Kim JY, Perez M. Experimental and Theoretical Studies on the Reaction of H<sub>2</sub> with NiO: Role of O Vacancies and Mechanism for Oxide Reduction. *Journal of the American Chemical Society* 2001;124:346.
- [8] Kung HH. *Transition Metal Oxides: Surface Chemistry and Catalysis*. New York: Elsevier, 1989.
- [9] Yin M, Wu C, Lou YB, Burda C, Koberstein JT, Zhu YM, O'Brien SJ. Copper oxide nanocrystals. *Journal of the American Chemical Society* 2005;127:9506.
- [10] Pena O, Pal U. Scattering of electromagnetic radiation by a multilayered sphere. *Computer Physics Communications* 2009;180:2348.
- [11] Palik ED. *Handbook of Optical Constants of Solids*: Elsevier, 1998.
- [12] Averitt RD, Westcott SL, Halas NJ. Linear optical properties of gold nanoshells. *Journal of the Optical Society of America B* 1999;16:1824.
- [13] Aspnes DE. Optical Properties of Thin Films. *Thin Solid Films* 1982;89:249.
- [14] Svoboda J, Fischer F, Vollath D. Modeling of formation of binary-phase hollow nanospheres from metallic solid nanospheres. *Acta Materialia* 2009;57:1912.
- [15] Svoboda J, Turek I, Fisher F. Application of the thermodynamic extremal principle to modeling of thermodynamic process in material sciences. *Philosophical Magazine* 2005;85:3699.
- [16] Perinet F, Barbezat S, Monty C. New investigation of oxygen self-diffusion in Cu<sub>2</sub>O. *Journal de Physique Colloque* 1980;C6:318.
- [17] Peterson N, Wiley C. Diffusion and point defects in Cu<sub>2</sub>O. *Journal of Physics and Chemistry of Solids* 1984;45:281.
- [18] Moore W, Selikson B. The Diffusion of Copper in Cuprous Oxide. *Journal of Chemical Physics* 1951;19:1539.



## Chapter IV – Shape Control of Cu Nanoparticles via Ligand Selection

### Introduction

Shape control at the nanoscale is critical for the use of metal nanoparticles for spectroscopy, catalysis, and plasmonic devices<sup>1</sup>. Within these applications, control of nanoparticle morphology will dramatically improve the ability to tune the material properties or novel materials for specific applications. Specifically, structural control will allow for improved selectivity for catalysts<sup>2,3</sup>, improved signal in spectroscopic applications<sup>4</sup>, and increased performance for plasmonic devices<sup>4,5</sup>.

Three metals which are commonly used for these applications are gold, silver, and copper. All three of these metals have a face-centered cubic (FCC) crystal structure. For single crystal FCC materials at the nanoscale, surface energy tends to dominate the thermodynamics of morphological control, which leads the structure to consist mostly of the lowest energy facets<sup>6</sup>. Thus the only shapes which are likely to form are bound by the lower energy (100) and (111) facets at the surface of the particle<sup>1</sup>. These shapes range from cubes (100) to octahedra (111) with one facet bounding the entire particle to cuboctahedra which is bound by both (100) and (111) facets. There also exist a subset of more anisotropic shapes which may be formed from single crystalline FCC materials such as rods, platelets, and tetrahedra<sup>1</sup>. Control of the final morphology of nanoparticles of silver and gold has been achieved through various synthetic methods, but shape control for copper nanoparticles is still relatively underdeveloped compared to silver and gold<sup>1,7-10</sup>.

Despite the fact that synthetic shape control is far less developed for copper than for silver and gold, copper is one of the most promising materials for useful applications of nanotechnology in industry. Copper's low cost, high electrical conductivity and useful optical properties make it an ideal candidate for many common applications when compared to silver or gold, which are orders of magnitude more expensive.

Previous work on synthetic routes to copper nanoparticles has shown that for the synthesis of spheres via multiple routes, the ratio of ligand to copper precursor has a positive relationship with average nanoparticle size<sup>11,12</sup>. In this work, we show a novel route to the synthesis of several different shapes of Cu nanoparticles by demonstrating that at the extreme range of this ratio, the large excess of ligands starts to exhibit shape control over the resulting nanoparticles which allows for the synthesis of Cu cubes and octahedra.

## Materials and Methods

Cube and platelet synthesis: All materials were ordered from Sigma-Aldrich or PCI Synthesis and used without further modification. Following the general synthetic template of O'Brien and coworkers<sup>11</sup>, but using a much higher ligand to copper ratio, 1.78 g of Oleic acid (90%, technical grade), or 1.79g of Stearic Acid (99%) was added to 6.06 g of trioctylamine (TOA, 98%) and 40 mg of copper (I) acetate (97%) in a three-necked flask in a nitrogen glovebox. The solution was kept at 50°C under vacuum for 30 minutes to degas in a standard Schlenk line setup. Following degassing, the solution was placed under nitrogen and quickly heated to 180°C and held for 55 minutes during which the color changed from forest green to yellow and finally to brown. Finally, the solution was heated quickly to 260°C for 30 minutes yielding a pink/dark red colloidal suspension of copper nanoparticles.

Octahedron synthesis: Nanoparticles were synthesized as previously shown by Ling et al<sup>12</sup>, but with much higher ligand to copper ratio. Briefly, .5 mmol of tetradecylphosphonic acid (TDPA) was combined with 10 ml TOA and .15 mmol copper (I) acetate and degassed for 30 minutes as discussed above. The solution was then placed under nitrogen and quickly heated to 180C for 55 minutes and 260C for 30 minutes, yielding a dark red colloidal suspension.

All nanoparticle solutions were stored in a nitrogen glovebox and size selected using centrifugation at 500 rpm for 1 minute in toluene. Following centrifugation, the supernatant was discarded and the solid phase was redispersed in toluene by sonication prior to further characterization.

TEM/HRTEM: Nanoparticle solutions were suspended in toluene and drop cast onto carbon-coated TEM grids. The TEM grids were then annealed at 275°C for 2 minutes in a nitrogen environment to remove excess organic material prior to being imaged.

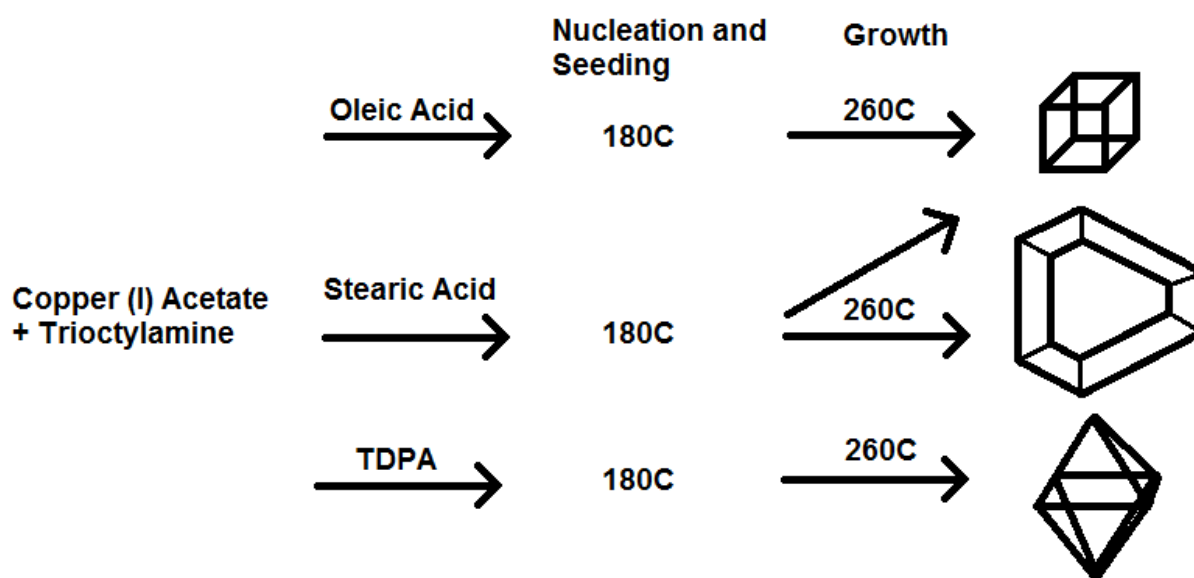


**Figure 1:** Synthesis scheme for the synthesis of Cu cubes, platelets, and octahedra. By keeping all conditions identical except the capping ligand, shape control is achieved.

## Results and Discussion

### Cubes

Cu nanocubes were observed in the oleic acid synthesis along with polydisperse spheres when the molar ratio of CuOAc to Oleic Acid was reduced to 1:20 as shown in Figure 2a. For a face-centered cubic (FCC) single crystalline material, a cubic structure may only be formed if the particle is bound by (100) facets. Since we know that these nanoparticles are made up of FCC copper, the cubic geometry shown in Figure 2a indicates that the exposed crystal plane must be the (100) face. This is a similar conclusion to Jin et al.<sup>13</sup> who found that their Cu cube synthesis resulted in structures bound on all sides by the (100) plane. In their work, Jin et al proposed that cube formation was the result of oxidative etching during the seed nucleation phase which results in a large shift of the distribution of seeds towards single-crystalline seeds instead of pentatwinned seeds. Similar cubic structures obtained with silver are also thought to be formed due to oxidative etching as demonstrated by Tao et al and Sun and Xia<sup>5,7</sup>. Our synthesis is performed in air free conditions without an etching agent, so it is reasonable that our final yield of cubes is lower than that of Jin et al.<sup>13</sup> because of the lack of selection towards single crystalline seeds. Due to the lack of an etching agent in our synthesis, a new mechanism must be proposed for the preference towards the (100) facets.

The primary question at hand is why do are cubes formed in this system at high particle sizes and high ligand concentrations, whereas spheres or cuboctahedra are formed for smaller particle sizes and lower ligand concentrations <sup>11</sup>.

From the cuboctahedra synthesis of O'Brien and coworkers<sup>11</sup> it is clear that the binding energy for oleic acid on the (100) and (111) surfaces are similar for small particles because experimentally we see no significant preference for one over the other. When the particle size is increased via an increase in ligand concentration, we see a strong preference for the (100) facet. Feichtenschlager et al. previously showed on  $\text{ZrO}_2$  and  $\text{SiO}_2$  particles that ligand alkyl chain ordering increased with particle size <sup>14</sup>, therefore decreasing the entropy of the ligands with increasing particle size. Our system should display similar behavior in which the entropy of the ligands decreases with increasing particle size. From previous studies on oleic acid self-assembled monolayers (SAMs) we know that oleic acid adsorbs in a monodentate configuration on the (100) surface <sup>15</sup> and in a bidentate configuration on the (111) surface <sup>16</sup>. With all other things being equal, increasing the order of ligands will have a more significant impact on the entropy of ligands bound in a bidentate configuration than those bound in a monodentate configuration because at higher ordering of the ligands on the surface the bidentate bound species will have fewer degrees of freedom than the monodentate bound species. Therefore, we suggest that the entropic penalty of the oleic acid ligands bound in a bidentate configuration on the (111) facet decreases the binding energy relative to the monodentate bound (100) facet enough to cause a preference towards stabilizing (100) facets and growth on (111) facets.

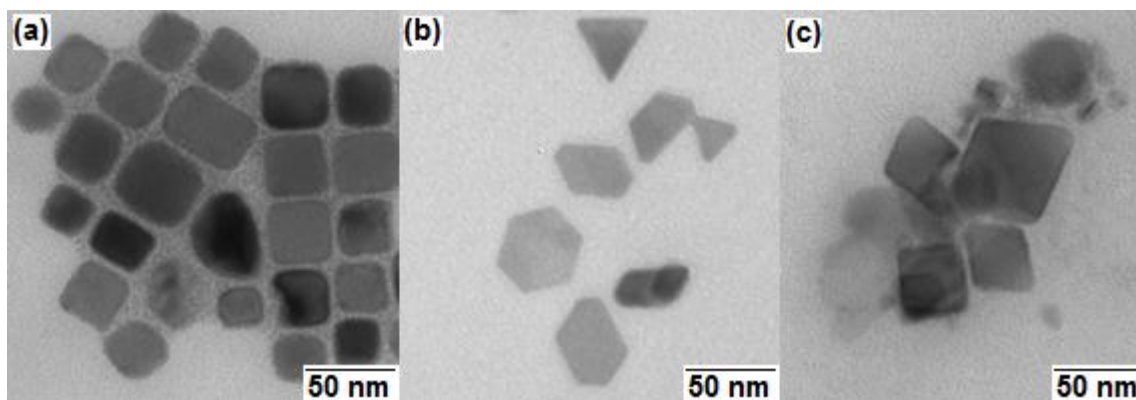


**Figure 2: Cubic and Octahedral Cu nanoparticles which were synthesized with oleic acid (a, cubes) and TDPA (b, octahedral).**

### Octahedra

Cu Octahedra were observed for the TDPA synthesis when the molar ratio of Cu precursor to capping ligand was decreased to 1:3 as shown in Figure 2b. Octahedral geometry is the predicted morphology of a FCC metal which is bound completely by the (111) facet<sup>1</sup>. The octahedra look similar to cubes in the TEM images except they contain two obtuse angles and two acute angles as seen in Figure 1b.

Baker et al. previously found that for alkanephosphonate SAMs, which are very similar to the TDPA used in this study, the alkyl chain orients nearly perpendicular to the crystal face on (111) Cu, implying that the phosphonate bonds in a tridentate configuration on the surface<sup>17</sup>. Thus for the observed structure shown in Figure 2b, we can infer that the particle is bound by the (111) facets on all sides and that the ligand is primarily bound in a tridentate configuration. The 3-fold symmetry of this bonding structure is similar to citric acid bonding on FCC silver as studied by Kilin et al.<sup>18</sup> where it was found that the three-fold symmetry of citric acid matched up well with the lattice spacing of the (111) face of silver, but not with the (100) face, resulting in a four-fold difference in binding energy. In the TDPA-Cu system, we see a similar mismatch with the geometry of the TDPA ligand and the (100) face contrasting against a good match with the symmetry and spacing of the (111) face. This mismatch is shown in Figure 3. The lattice spacing between neighboring Cu atoms for both faces is 2.6 Å, but the configuration is cubic on the (100) face and hexagonal on the (111) face. For TDPA in a tridentate bonding configuration assuming tetrahedral geometry and P-O bond lengths of 1.54 Å, the distance between neighboring oxygen atoms is 2.52 Å. This similarity in geometry given by the 3-fold symmetry and similar bond lengths allows the TDPA to bond using all three oxygen atoms which are naturally oriented almost identically to the surface Cu atoms as shown in Figure 3. Future computational work will be needed to confirm this difference in binding energy, but combined with the similarity to the citric acid/Ag (111) system<sup>18</sup> it seems reasonable to conclude that this lattice matchup could explain the preference of the TDPA ligand for the (111) facet at high concentrations.

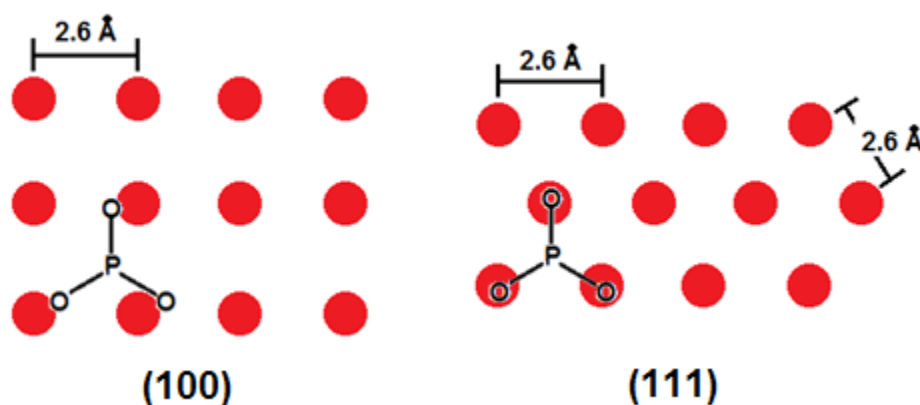


**Figure 2: (100) and (111) surface planes of FCC copper with top-view of the phosphonic acid ligand deprotonated and bound in a tridentate configuration with the alkyl chain removed for clarity.**

On the other hand in a similar silver system, Tao et al show that the transition between cubic and octahedral morphology is kinetically determined instead of thermodynamically<sup>5</sup>. In their work, cubic

and octahedral particles were both synthesized in the presence of PVP, a ligand most commonly thought to have a preference for the (100) facet in silver. They showed that cubic nanoparticles transition into cuboctahedral and then octahedral nanoparticles with increasing reaction time, shedding doubt on the idea that preference of the ligand for a particular facet is the only important driving force for shape selectivity, but instead factors like temperature, reactant concentration, and reactant molar ratios might be more important<sup>5</sup>.

### Platelets

Finally, Cu platelets were synthesized in the presence of stearic acid at a ligand to copper mole ratio of 20:1. The crystal structure of platelets for a FCC metal consist of the (111) face on the top and bottom of the platelet and the edge being made up of the (100) and (111) family of planes<sup>10</sup>. This is in contrast to the mechanism proposed above for cube synthesis which predicts that carboxylic acid ligands should have an affinity for the (100) plane at high concentrations and particle sizes. The difference between stearic acid and oleic acid, however, is the double bond in the middle of the alkyl chain. Stearic acid should have a straight conformation, whereas oleic acid has a bend in the middle of the chain due to the cis-double bond, giving it a boomerang shape. It is unclear at this time the exact nature of the alkyl chain's contribution which drives the formation of platelets instead of cubes, but a likely avenue for future investigation is the contribution of the straight alkyl chain's packing on the flat surface of the platelet compared to oleic acid's bent alkyl chain. Further work is necessary to concretely pin down a mechanism for platelet formation.

### Conclusion

In this work, a general colloidal synthetic procedure was developed with a very high ligand to copper precursor ratio that allows shape control by changing the coordinating ligand between TDPA, oleic acid, and stearic acid. It was demonstrated from the final morphology of the particles that TDPA has a stronger affinity for the (111) facet whereas oleic acid bonds more strongly to the (100) face, and stearic acid produces a structure with both faces, but with a flat platelet morphology. A mechanism was proposed suggesting that cube formation was entropically favored at high concentrations of oleic acid due to bidentate bonding on the (111) facet and monodentate bonding on the (100) facet, and that octahedral formation was enthalpically favored for high concentrations of TDPA due to a higher bonding energy caused by a good alignment of the phosphonic acid ligand with the (111) Cu facet. Future work will focus on identifying a concrete mechanism for the formation of platelets in stearic acid and quantitatively verifying the cube and octahedra mechanisms by DFT analysis. Additional future work will attempt to quantify the contributions of the other synthetic parameters such as time, temperature, reactant concentration, and reactant ratios on size and shape control.

### References

- (1) Tao, A. R.; Habas, S.; Yang, P. **2008**, 4, 310.
- (2) Zhou, X.; Gan, Y.; Sun, S. *Acta Physica-Chimica Sinica* **2012**, 28, 2071.
- (3) Cho, H.-J.; Hwang, P.-G.; Jung, D. *Journal of Physics and Chemistry of Solids* **2011**, 72, 1462.
- (4) Pastoriza-Santos, I.; Sanchez-Iglesias, A.; Rodriguez-Gonzalez, B.; Liz-Marzan, L. M. *Small* **2009**, 5, 440.
- (5) Tao, A.; Sinsermsuksakul, P.; Yang, P. *Angew. Chem. Int. Ed.* **2006**, 45, 4597.
- (6) Soon, A.; Wong, L.; Delley, B.; Stampfl, C. *Physical Review B* **2008**, 77, 125423.
- (7) Sun, Y.; Xia, Y. *Science* **2002**, 298, 2176.
- (8) Jin, M.; He, G.; Zhang, H.; Zeng, J.; Xie, Z.; Xia, Y. *Angewandte Chemie International Edition* **2011**, 50, 10560.
- (9) Averitt, R. D.; Westcott, S. L.; Halas, N. J. *Journal of the Optical Society of America B* **1999**, 16, 1824.
- (10) Maillard, M.; Giorgio, S.; Pileni, M.-P. *Journal of Physical Chemistry B* **2003**, 107, 2466.
- (11) Yin, M.; Wu, C.-K.; Lou, Y.; Burda, C.; Koberstein, J. T.; Zhu, Y.; O'Brien, S. *Journal of the American Chemical Society* **2005**, 127, 9506.
- (12) Hung, L. I.; Tsung, C. K.; Huwang, W.; Yang, P. *Advanced Materials* **2010**, 22, 1910.
- (13) Jin, M.; He, G.; Zhang, H.; Zeng, J.; Xie, Z.; Xia, Y. *Angewandte Chemie International Edition* **2011**, 50, 10560.
- (14) Feichtenschlager, B.; Lomoschitz, C. J.; Kickelbick, G. *Journal of Colloid and Interface Science* **2011**, 360, 15.
- (15) Dubois, L. H.; Zegarski, B. R.; Nuzzo, R. G. *Langmuir* **1986**, 2, 412.
- (16) Wuhn, M.; Weckesser, J.; Woll, C. *Langmuir* **2001**, 17, 7605.
- (17) Baker, M. V.; Jennings, G. K.; Laibinis, P. E. *Langmuir* **2000**, 16, 3288.
- (18) Kilin, D. S.; Prezhdo, O. V.; Xia, Y. *Chemical Physics Letters* **2008**, 458, 113.

## Chapter V – Conclusion and Future Work

In this work, we have demonstrated the ability to tune the morphology of copper and copper oxide nanoparticles via three distinct methods: oxidation, reduction, and synthetic control. The lessons learned in this work may be applied across several fields to improve the performance of many different systems which utilize copper or copper oxide nanoparticles as working materials.

In the first part of this work we demonstrated the ability to tune hollow  $\text{Cu}_2\text{O}$  nanoparticle void size by changing oxidation conditions in a predictable fashion. This could in turn lead to improvements in catalytic performance for  $\text{Cu}_2\text{O}$  catalysts which are commonly used for the water-gas shift reaction or for methanol synthesis. In addition, the model developed in this process is capable of being generalized to any material which could lead to the improved ability for researchers to characterize and predict the behavior of novel nanomaterials.

Next we changed our focus to the reduction of  $\text{Cu}_2\text{O}$ . Through the use of in-situ UV-Vis spectroscopy, we showed that the intermediate state of a  $\text{Cu}/\text{Cu}_2\text{O}$  nanoparticle looks remarkably similar to the intermediate state of the oxidation process with a metal core and an oxide shell due to the short diffusion length of the nanoparticle system. This is in stark contrast to bulk reduction mechanisms in which an advancing interface of metal/reduced oxide comes from the surface downward.

In the final chapter we discussed progress to date on developing novel synthetic routes to uniquely shaped copper nanoparticles. Specifically we synthesized copper cubes, octahedral, and platelets by changing the coordinating ligand. Mechanisms for the shape control were proposed in each case, but need to be quantified further by computational work in order to prove their validity.

### Future Work

In this thesis we explored several aspects of the  $\text{Cu}/\text{Cu}_2\text{O}$  system, but many more avenues for investigation still remain.

When working with the  $\text{Cu}$  nanocubes discussed in Chapter 2, it was observed that when the cubes oxidize, they become either highly porous or form a cubic void depending on oxidation conditions. This is a highly unexpected result, as isotropic diffusion during the oxidation process should lead to non-cubic final morphologies in an oxidized particle in accordance with our work on the nanoscale Kirkendall effect discussed in Chapter. Figure 1 shows an example of a nanoporous  $\text{Cu}_2\text{O}$  cube which was formed by 3 cycles of oxidation at 200C for 20 minutes on a carbon coated TEM grid with imaging performed between each subsequent oxidation.



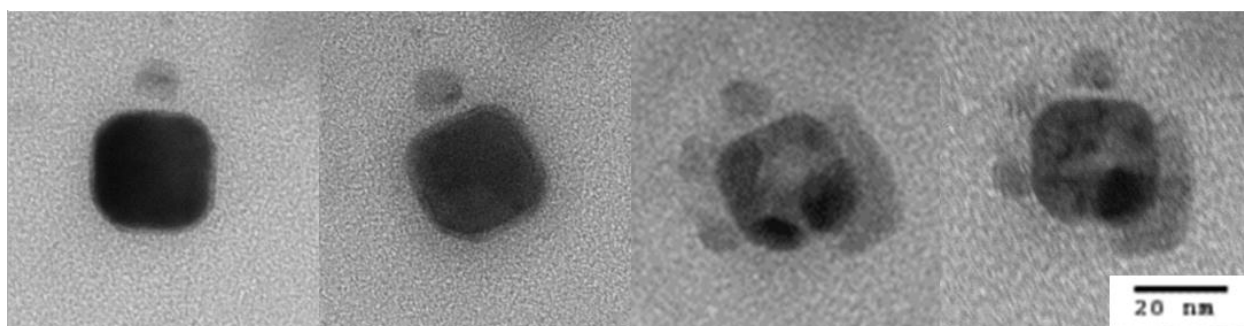


**Figure 1: TEM images of sequential oxidation of a single Cu nanocube to  $\text{Cu}_2\text{O}$ . From left to right, between each subsequent image the TEM grid was oxidized in ambient air at 200C for 20 minutes. After the second oxidation, large pores appeared in the center of the particle and material diffused to the outside border of the porous cube.**

When oxidation was performed in solution on the other hand, cubic voids were observed in the hollow  $\text{Cu}_2\text{O}$  particles. Figure 2a shows a striking example of a hollow  $\text{Cu}_2\text{O}$  nanobox which lies immediately next to an unoxidized Cu cube which demonstrates the morphological change that occurs during oxidation. It can be inferred from this image that oxidation in solution is a stochastic process which takes a non-negligible amount of time to initiate, but occurs relatively quickly following initiation of the reaction, thus allowing both unoxidized cubes and hollow oxide nanoboxes to exist in the same solution for relatively short oxidation times. Figure 2b shows the ability for the hollow nanocubes to self-assemble into large area lattices which are highly porous with cubic voids within each particle. These lattices could potentially be useful for catalytic applications as their well-defined pores allow for improved selectivity by their use as a diffusion barrier.

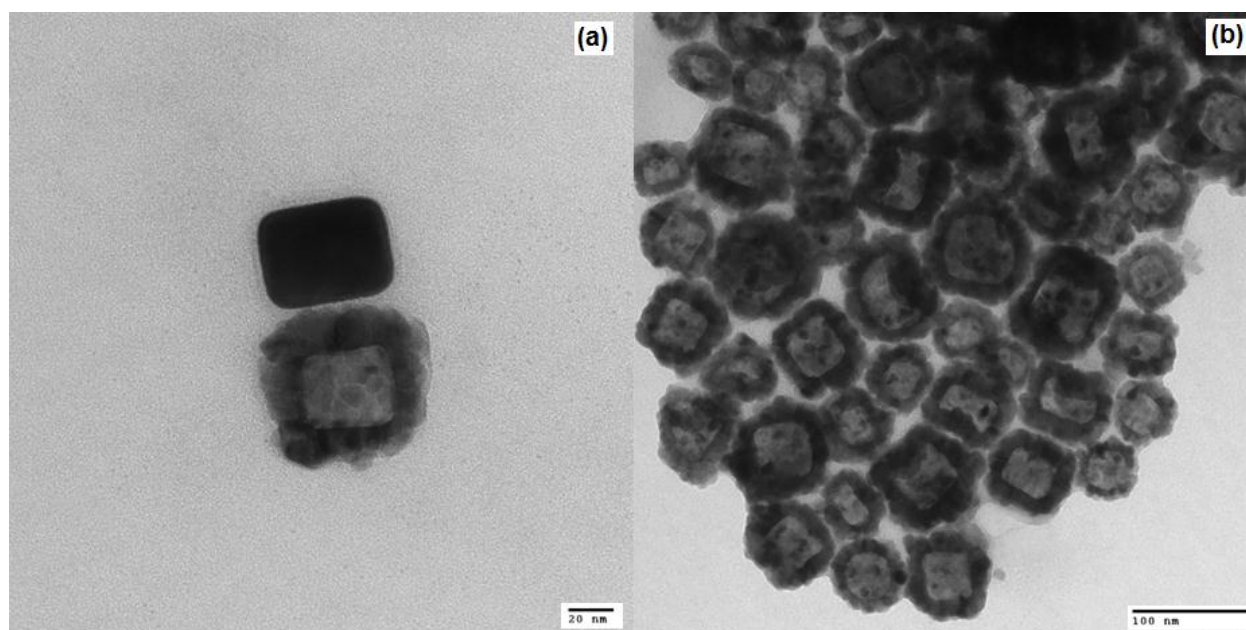


**Figure 2: TEM images of Cu cubes oxidized for 1 day at room temperature in hexane. The two cubes shown in (a) demonstrate that for short oxidation times solid Cu cubes exist in solution with fully oxidized hollow Cu<sub>2</sub>O cubes. (b) shows a matrix of hollow Cu<sub>2</sub>O cubes that has self-assembled over a reasonably large area which could be useful for forming highly porous super-lattices which could be used for catalytic applications or for solar cells.**

Future investigations could focus on combining these preliminary oxidation results with the results of chapter 4 with the goal of obtaining hollow particles of any arbitrary shape and/or size. These results would be of interest for applications in catalysis with the hope that improved shape control could improve selectivity of various reactions.

# Appendix A: Origin of the Optical Properties of Noble Metals

## I: Introduction

Optical properties describe and quantify the interactions of light and matter. Specifically, they quantify reflection, refraction, absorption, and transmission at any given frequency for a given material. The origin of optical properties lies in a materials electronic and crystalline structure. In particular, the behavior of the “free” conduction electrons mostly determines optical properties at low energies, the band structure of a metal determines the behavior at high energies, and at intermediate energies a mixture of the two effects dominates. This behavior may be quantified by examining a material’s frequency dependent complex dielectric function. The real component of the dielectric function roughly characterizes the polarizability of a material, whereas the imaginary component characterizes its absorption and scattering behavior.

Single element materials in the same column in the periodic table often show mutually similar properties such as alkali metals and halogens; the same may be said for the optical properties of the noble metals gold, silver, and copper in group 11 despite their very different reactivities. In this paper, the discussion will focus on the dielectric functions of noble metals in group 11; copper, silver, and gold.

## II: Free Electron Model

In undergraduate courses, band structures of metals, semiconductors, and insulators are typically presented as a simplified diagram such as the one shown in Figure 1. In this diagram, a material will conduct electricity if there are open states directly above the Fermi level or if an electron is excited into the conduction band.

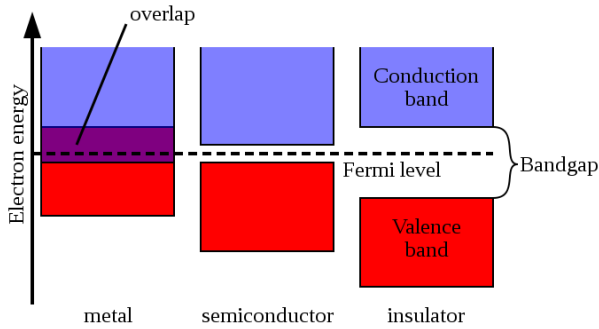


**Figure 1: Simplified diagram of band structures used to demonstrate the difference in conductivities between metals, semiconductors, and insulators. Figure taken from [1].**

For metals, the conduction and valence bands both overlap with the Fermi level which means that they will always conduct electricity due to the continuous band of available, unoccupied states just above the Fermi level. These electrons which occupy the conduction band in their ground state are referred to as conduction band electrons or free electrons. The idea that a few of the electrons near the Fermi level are responsible for the conductive properties of metals gives rise to the Drude model of free electron behavior. The Drude model is a straightforward way to roughly estimate the optical properties of a metal by modeling the metal as a cloud of free electrons. In this model, the core electrons are ignored and the metal is assumed to behave as a homogenous gas of electrons. The resulting equation for the complex dielectric function takes the form of Eq. 1 [2] where  $\epsilon$  is the frequency dependent complex dielectric function,  $\omega_{pa}$  is the experimentally determined plasma frequency, and  $\tau_c$  is a constant associated with relaxation time of electrons in excited states in the metal.

$$\epsilon(\omega) = 1 - \frac{\omega_{pa}^2}{\omega + \frac{i}{\tau_c}} \quad \text{Eq. 1}$$

The results derived from this model are reasonably close to measured values at low energies (<2eV), but are a very poor approximation at higher energies because the model fails to account for the interactions of photons with non-conduction band electrons, such as the electrons in d or d-sp-hybridized orbitals. These electrons have energies close to the Fermi level which allows them to undergo interband transitions upon interaction with a photon of the appropriate energy. In other words, they cause the metal to behave like a semiconductor for energies above ~2 eV by absorbing and emitting photons by transitioning between neighboring energy bands. This sort of behavior leads to sharp inflection points and changes in slope within the dielectric functions at energies corresponding to common transitions. With this in mind, another level of complexity must be added to the traditional band structure diagram for metals

which takes into account the possibility of interband transitions at higher energies. With this in mind, detailed band structures have been calculated which may be used to qualitatively assign transitions between bands to various distinct characteristics at specific energies. The following section will focus on the methods and background necessary to analyze calculated band structures and their relationship to a material's optical properties.

### III: Band Structure of Noble Metals

#### Brillouin Zone

The Brillouin zone is a term used to mathematically describe a single species in a crystal lattice. It may be used to characterize properties of a lattice completely by describing the behavior of only a single Brillouin zone. It is easiest to visualize in two dimensions, as in Figure 2a. Starting from the center point, a line is drawn midway between each of its closest neighbors. The area enclosed by all of these lines is the Brillouin zone.

In three dimensions, the process for constructing the Brillouin zone is the same. Since gold, silver, and copper are all face-centered cubic metals, this discussion will focus on the FCC Brillouin zone from here on. The 3-d Brillouin zone for a FCC lattice is shown in Figure Figure c below. Several high-symmetry points are labeled by standardized variables.

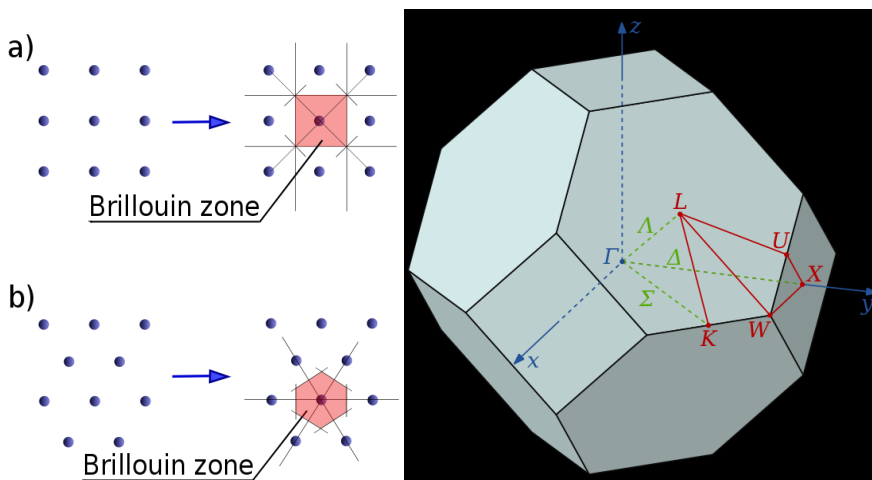


Figure 2: a-b) Derivation of the 2-d Brillouin zone for a cubic (a) or close-packed (b) lattice. c) The 3-d Brillouin zone for an FCC lattice. Points of high symmetry on the surface of the Brillouin zone are labeled with standardized variables such as  $\Gamma$  (the origin – (000)),  $X$  (center of the square face – (100)), and  $L$  (center of the hexagonal face – (.5,.5,.5)). Both figures taken from [3]

We are interested in the Brillouin zone because it is useful for describing energy levels and shapes of different bands in a material relative to the Brillouin zone. Later in this review, the band structure of Au, Ag, and Cu are discussed with each band plotted against points of high symmetry such as  $\Gamma$ ,  $X$ , and  $L$  in the Brillouin zone. Another closely related geometrical concept

which will be important to understanding the band diagrams of noble metals is the Fermi surface.

### Fermi Surface

By definition, the Fermi surface is a surface of constant energy (the Fermi energy) in  $k$  space. In real space, the Fermi surface is the surface of the orbitals that are occupied at 0K, or below which all available orbitals are occupied. A representation of the Fermi surface of copper is shown in Figure 3 below. One important feature to note about the Fermi surface of copper as well as the other noble metals is the “necks” which contact the boundary of the first Brillouin zone. The presence of these “necks” demonstrate a continuous path for charge carriers across the entire lattice and give rise to the high conductivity of the noble metals. The exact shape of the Fermi surface may be determined experimentally by taking advantage of the De-Haas van-Alphen effect (dHvA).

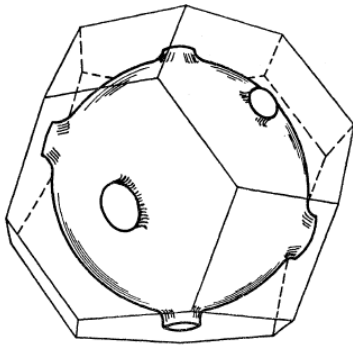


Figure 3: A sketch of the Fermi Surface for copper encased in the first Brillouin zone for a FCC crystal structure. Figure taken from [4]

### De-Haas van-Alphen Effect

The dHvA effect is a quantum mechanical phenomena in which the magnetic moment of a single crystalline pure metal oscillates in the presence of a strong external magnetic field [5]. The period of the induced oscillation is inversely proportional to the area of the Fermi surface perpendicular to the applied magnetic field [5]. It is important to note that this effect is only measurable at extremely low temperatures and very high magnetic fields (<50K and >13 Tesla). Quantitatively, the period of the oscillation is proportional to the cross sectional area of the Fermi surface normal to the magnetic field ( $S_e$ ) according to the following relationship [5].

$$P = \frac{1}{F} = \Delta \frac{1}{B} = \frac{2\pi e}{\hbar c} \frac{1}{S_e} \quad \text{Eq. 2}$$

Where  $P$  is the period of oscillation,  $F$  is the frequency of oscillation, and  $B$  is the strength of the magnetic field.

Knowing the exact shape of the Fermi surface allows detailed band calculations to be performed which allows for qualitative connections to be drawn between the dielectric function and the band structure for a given material. In the published literature, the Fermi surfaces of countless materials have been characterized.

### **Band Structures of Gold, Silver, and Copper**

As shown in Section II, the traditional band diagram for metals, semiconductors, and insulators is oversimplified and is not sufficient to explain the optical properties of metals at energies high enough to excite interband transitions. A more complicated model for gold, silver, and copper is presented below which will be useful to explain the optical behavior of these metals at all energies.

The band structure of gold is shown below as Figure 4. Gold has an electronic structure of  $[\text{Xe}]5d^{10}6s^1$  [6]. The states arising from the core orbitals are low in energy relative to the 5d and 6s states so they can be ignored for the purposes of this discussion. The 6 bands near the Fermi energy are plotted against several points of symmetry on the Brillouin zone (Figure b). There is some degree of s-d hybridization so it is difficult to assign a specific s or d character to each energy band, but a reasonable approximation would assign the flat bands below the Fermi level to 5d character with a small amount of s-hybridization and the remaining band that varies widely in energy above and below the Fermi level to mostly s character with a small amount of d-hybridization [6] [7]. The first thing to notice about Figure is that the Fermi surface for gold is similar to that of copper shown in Figure . We can see that the Fermi surface crosses the Brillouin zone along most of the WQL face as well as some of the  $\Gamma\Sigma K$  face. It is immediately apparent that gold should act as a good conductor because of the states that extend above and below the Fermi energy along the WQL and  $\Gamma\Sigma K$  directions, indicating a partially filled band. The shape of the orbitals below the Fermi surface may be used to predict the character of the dielectric constant in the region associated with interband transitions. For example, state 8 at the  $\Gamma$  point on the Brillouin zone has an energy of approximately .2 Rydberg (or 2.7 eV) below the Fermi Energy. Therefore, we could predict there to be an increase or change in the slope of  $\epsilon_2$ , which is associated with absorbance and scattering behavior, around 2.7 eV attributable to an interband transition from state 8 to an unoccupied state near the Fermi Energy. Furthermore, all of the higher energy transitions in the band structure at points of high symmetry may be assigned to different features on the plot of gold's dielectric function as will be shown in Section IV.

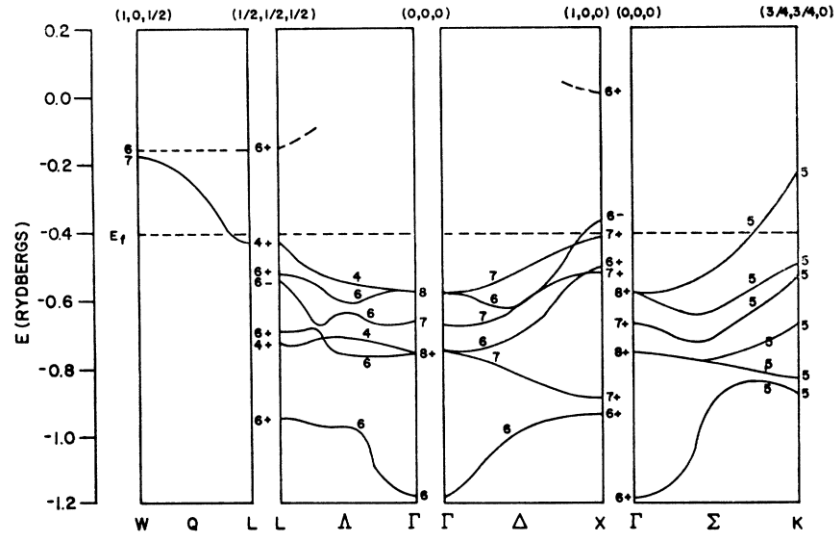


Figure 4: The calculated energy bands for Au along various symmetry axes in the Brillouin zone. Figure taken from [6].

Silver has an electronic structure of  $[\text{Kr}]4d^{10}5s^1$  [2]. As with gold, its band diagram has 6 bands near the Fermi level which are made up of the 5 4d bands and a 5s band. The degree of hybridization in silver's band structure is significantly less than gold as can be seen in silver's very flat d-bands and non-flat s-band. This has been recently confirmed experimentally by Sekiyama et al. who showed that the 5d electrons in gold have a significant contribution to the conduction band whereas in silver the 4d electrons contribute very little to the conduction band [7]. However, the 5s band still appears to be qualitatively similar to that of gold with the Fermi surface contacting the boundaries of the Brillouin zone around the WQL and  $\Gamma\Sigma K$  faces. Another major difference between gold and silver is that the flat d-bands are approximately 4 eV lower than the Fermi level, compared to about 2.7 eV lower for gold [2]. This has a major impact on the location of the onset of interband transitions for silver's dielectric function. Therefore it is expected that silver would exhibit free-electron behavior at higher energies than gold and have sharp changes in the dielectric function at around 4 eV as opposed to 2.7 eV for gold. This is confirmed by the experimentally measured dielectric function as shown in Section IV.





## Section IV: Experimental Determination of the Complex Dielectric Function

Shifting from theory to experiment, it is desirable to confirm the predictions gathered from the calculated band structures experimentally. Dielectric constants for a material may be calculated from reflectance measurements. The overall procedure for reducing experimental reflectance data into the real and imaginary dielectric constant as a function of wavelength is to first find the real and imaginary index of refraction from the reflectance data, then calculate the real and imaginary dielectric constants from refractive indices. An example of experimental reflectance data is shown in Figure 1 as near normal reflectance measurements for silver at 300K for 0 to 23 eV [2].

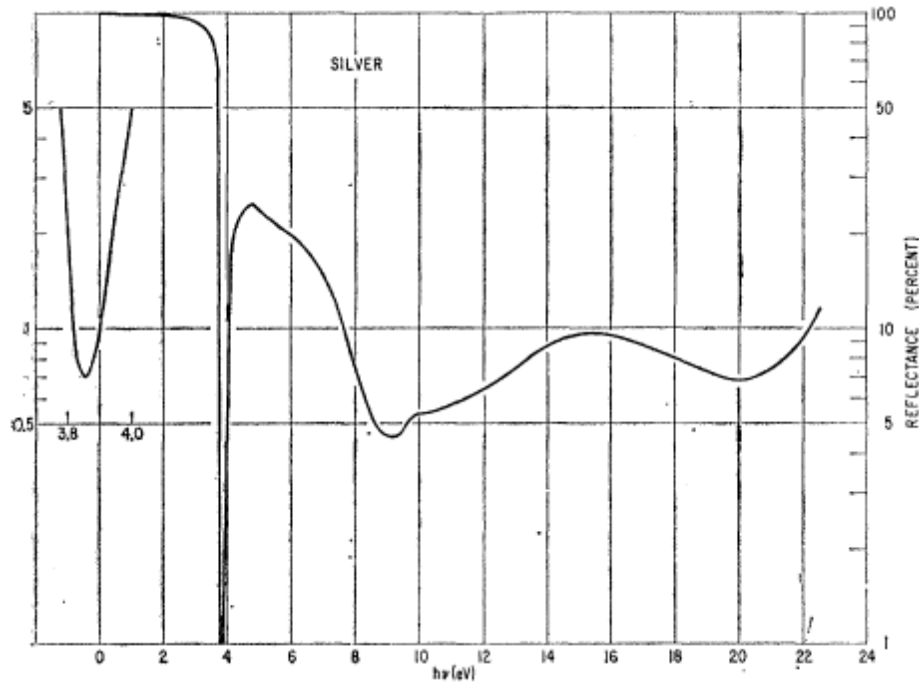


Figure 7: Experimental near normal reflectance data for an ultra-pure silver thin film. Note the extreme feature at 4 eV as a result of the first onset of interband transitions. This feature marks the upper end of the “free electron” region and the lower end of the interband transition region. Figure taken from [2].

Recall that reflectivity is related to the index of refraction of both materials at the interface. The exact nature of this relationship is shown in Equation 3, where  $n_2$  and  $n_1$  are the real components of the indices of refraction for the material and the medium, respectively.

$$R = \frac{n_2 - n_1}{n_2 + n_1} \quad \text{Eq. 3}$$

Using Equation 3, the real index of refraction may be calculated from experimental data. Once the real component of the index of refraction is known, the imaginary index of refraction  $k$  may be calculated using Kramers-Kronig relations. Kramers-Kronig relations are mathematical relationships that may be applied to any complex function which allows the imaginary component to be calculated from the real component and vice-versa [2]. Finally, using the complex refractive index,  $n + ik$ , the dielectric constant may be calculated using the following equations:

$$\epsilon_1 + i\epsilon_2 = (n + ik)^2 \quad \text{Eq. 4}$$

$$\epsilon_1 = n^2 - k^2 \text{ and } \epsilon_2 = 2nk \quad \text{Eq. 5}$$

The results of the above analysis of experimental data yields the complex dielectric functions shown in Figures Figure 8, Figure 9, and Figure 10

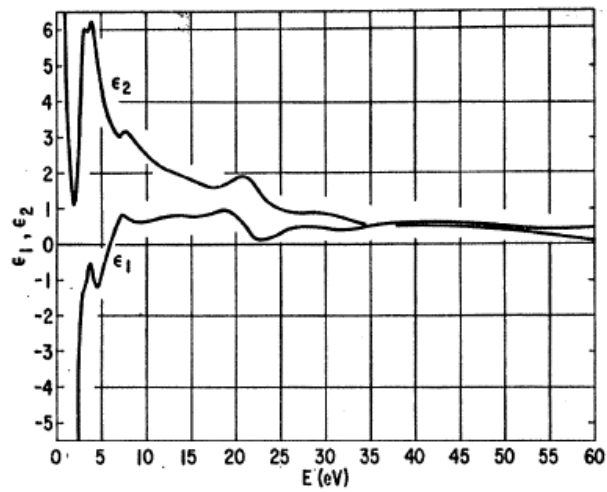


Figure 8: Complex dielectric function for Au. For Au, the onset of distinctive features occurs at approximately 2.7 eV. Figure taken from [6]

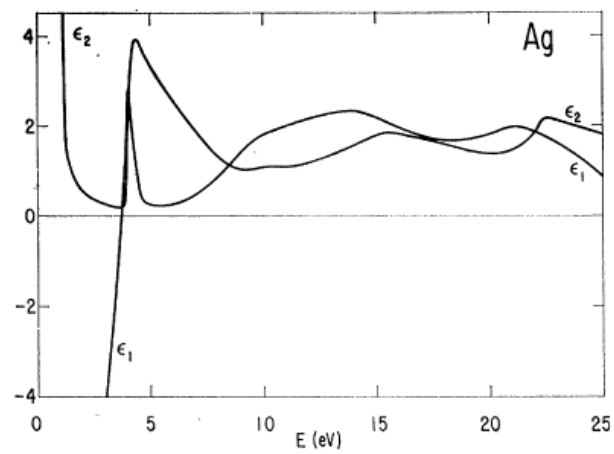
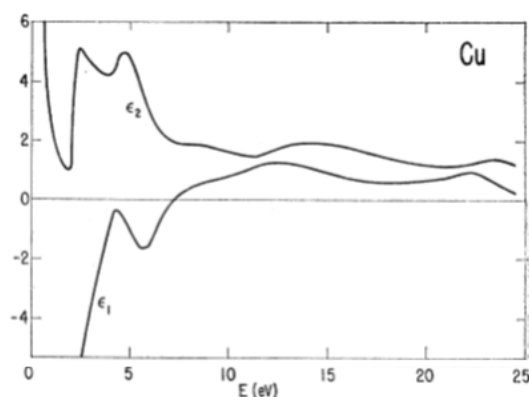


Figure 9: Complex dielectric function of Ag. For Ag, the onset of distinctive features occurs much higher than gold at approximately 4 eV. Figure taken from [2].



**Figure 10: Complex dielectric function of Cu.** The onset of distinctive features for Cu occurs at around 2.2 eV. Overall the dielectric function for Cu appears much more similar to Au than to Ag. Figure taken from [2].

As shown in Section III, the onset of distinctive features in each of the dielectric functions begins at the same energy as the onset of interband transitions; 2.7 eV for Au, 4 eV for Ag, and 2.2 for Cu. The remainder of the spectrum is a reflection of the number of accessible interband transitions as well as the relaxation time for electrons which are excited to those states [2]. Having established a foundation in these properties, the discussion will now turn to a particular application for the optical properties of noble metals.

### Section V: Plasmonics

A relatively new field closely related to the optical properties of noble metals which has grown in popularity and impact over the last decade is plasmonics. The field of plasmonics takes advantage of the collective resonance of free electrons at the metal-dielectric interface in certain nanostructured materials to create a large absorbance at resonance frequencies as well as a large increase in the local electric field. A simplified example of this effect is shown in Figure 11.

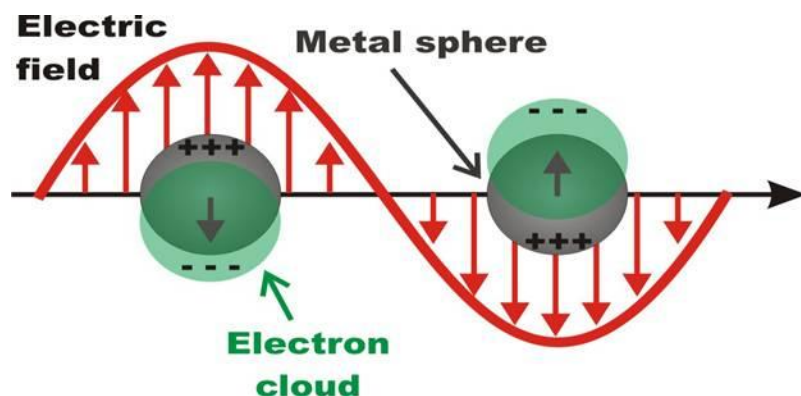


**Figure 11: Diagram showing the collective oscillation of free electrons in a metal nanosphere.** Figure taken from [8].

The resonance stems from coherent oscillation of the conduction band electrons with the incident photons at the metal-dielectric interface. The frequency at which this resonance occurs is dependent on four factors: electron density, effective electron mass, and the shape/size of the Fermi surface in the material [9]. The name for this effect is plasmon resonance. There are two commonly used and closely related applications of this effect known as surface plasmon resonance (SPR), in which the electromagnetic wave created by the plasmon resonance propagates parallel to the metal-dielectric interface, and localized surface plasmon resonance (LSPR), in which the electromagnetic field oscillates locally around a nanoparticle of particular geometry and size. For the purposes of this review, the terms will be used interchangeably because though they differ in size scales, they stem from the same phenomena.

Plasmons are useful for a variety of different applications because of the large enhancement of the local electric field and large increase in absorbance at specific frequencies. Specific applications include chemical and biological sensors, surface enhanced Raman scattering spectroscopy, near-field scanning optical microscopy, and optical energy transport [9] among many others.

Traditionally SPR and LSPR research has focused on gold and silver because of their strong plasmon resonance and relatively inert character. Recently copper has started to gain some popularity in the field because it also has a strong SPR signal (though not as strong as gold and silver), but its practical uses are limited due to its strong tendency to oxidize under atmospheric conditions. It has another limitation which is related to the interband transitions discussed in Section III. For gold and silver, the plasmon resonant energies are well below the interband transition energies, so they may be treated as free electron systems [10]. For copper, on the other hand, the plasmon resonance for copper nanospheres occurs near 2.2 eV which means that the intensity of the plasmon will be damped by interband transitions which occur at the same energy. As a result of this overlap, copper has a much less intense plasmon resonance than silver or gold. On the other hand, for certain geometries of copper such as nanoshells, the plasmon resonance peak shifts to lower energies which leads to a two-peaked absorption spectrum [10].

Other metals have been shown to exhibit SPR behavior, but have not been as widely studied because their SPR peaks are not as strong as those displayed by the group 11 metals. Table 1 below contains a list of different metals that have demonstrated plasmonic behavior as well as their potential applications.

No.	Metal	Application	Metal Thickness, nm	SPCL Wavelength Range, nm	SPCL Observation Angle	Reference
1	Chromium	Fluorescence	20	276-517	Variable: 50-80	NP
2	Aluminum	Fluorescence	20	280-600	Variable: 42-46	NP
3	Palladium	Fluorescence	15/20	300-800	Variable: 45-70	NP
4	Zinc	Fluorescence Chemiluminescence	30	305-545	Variable: 45-68 Variable: 30-60	12
5	Nickel	Fluorescence Chemiluminescence	15/20	344-1240	Variable: 50-70 Variable: 50-70	15
6	Rhodium	Fluorescence	15	344-1240	Variable: 45-75	NP
7	Silver	Fluorescence Chemiluminescence	40	413-620	Variable: 45-60	17
8	Gold	Fluorescence Phosphorescence	50	496-886 650	Variable: 45-60 65	10,13
9	Iron	Fluorescence Chemiluminescence	15	496-886	Fixed: 65 Fixed: 65	NP
10	Copper	Fluorescence	40	521-659	Variable: 55-70	18
11	Platinum	Fluorescence	15	800-1500	Variable: 50-70	NP

<sup>a</sup> NP-not published.

Table 1: A list of some common metals and their plasmonic characteristics. Taken from [11].

### Size dependence of the plasmon resonance wavelength

The LSPR behavior of metal nanospheres is well characterized using the Mie solution to Maxwell's equations. The Mie solution takes the form of an infinite series solution, but in the simple case of nanospheres the extinction coefficient can be simplified to Eq. 6.

$$\sigma(\lambda) = \frac{18\pi V \epsilon_m^{\frac{2}{3}}}{\lambda} * \frac{\epsilon_2}{(\epsilon_1 + 2\epsilon_m)^2 + \epsilon_2^2} \quad \text{Eq. 6}$$

Where  $\sigma$  is the absorption cross-section which is directly proportional to extinction,  $V$  is the volume of the particle,  $\lambda$  is the wavelength of incident light, and  $\epsilon_m$ ,  $\epsilon_1$ , and  $\epsilon_2$  are the wavelength dependent dielectric functions of the medium and copper, respectively. One important takeaway from this solution is that the peak of the extinction spectra will be at its maximum value when  $\epsilon_1 + 2\epsilon_m = 0$ . Therefore, the plasmon peak in a system is highly dependent on the solvent in which the nanoparticles are dispersed. In general because of the size effects associated with the behavior of Drude electrons at small particle sizes, an increase in particle size will blue-shift the plasmon peak and a decrease will red-shift the peak. Following the Mie solution, and in the limit of nanospheres diameters less than 50 nm and in solvents with dielectric constants between 1 and 3, Cu nanospheres will have a LSPR peak around 580-620 nm, silver will have a LSPR peak around 380-420 nm, and gold will have a LSPR peak around 530-570 [10].

The limit chosen above for the characteristic frequencies for each material is the size at which the plasmon resonance is associated with only dipole oscillations. At larger particle sizes, or in nanoshells with shells thicker than approximately 30 nm, another oscillation mode known as the quadrupole mode appears. Quadrupole and dipole oscillations are shown as a change in local electric field in Figure 12. For systems in which both the dipole and quadrupole resonance are significant, the absorbance spectrum may exhibit a broad peak which is a combination of two peaks separated by a few nanometers as shown in Figure 13 [10].

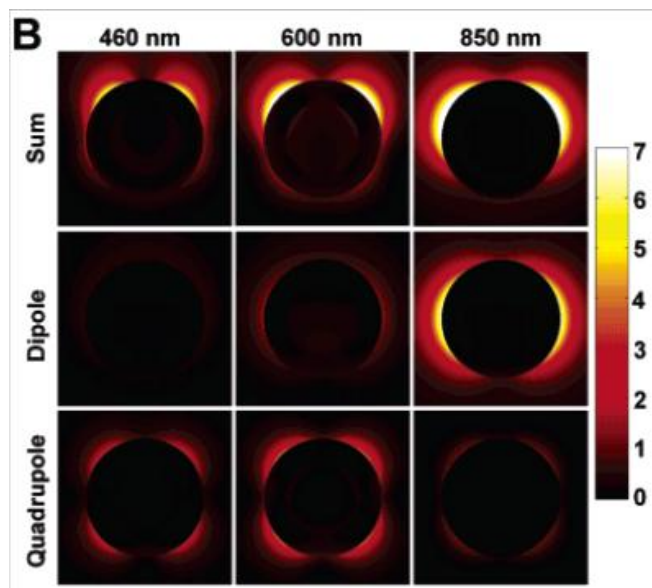


Figure 12: A theoretical plot of the change in magnitude of the electric field around a copper nanoshell due to localized surface plasmon resonance in the dipole and quadrupole modes. The color bar indicates magnitude of  $|E^2|$ . Figure taken from [10].

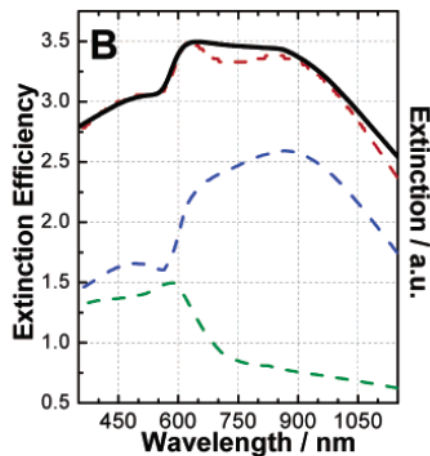


Figure 13: Extinction spectra for Cu nanoshells with a silica core of radius 63 nm and a shell thickness of 45 nm in ethanol. The red curve is theoretically calculated with Mie solution calculations, the green curve is the theoretical absorbance



spectrum, the blue curve is the theoretical scattering spectrum, and the black curve is the experimentally measured extinction spectra. Figure taken from [10].

### Shape dependence

Through experimental and theoretical treatments, the plasmonic character of various shapes such as spheres, shells, rods, and quantum dots have been well characterized [12]. In general, these shapes follow the same rules as spheres for shifts in the LSPR peak for changes in size. Increasing characteristic length leads to a blue shifted peak, and vice versa. However, for structures with more than one characteristic length such as rods, the spectrum will show two LSPR peaks; one corresponding to the axial dimension and the other corresponding to the lateral dimension [12].

As structures become more complicated, the Mie solution is no longer able to produce a theoretical solution for the system's plasmon resonance. Alternatively, a relatively simple model may be used to analyze the structure's plasmon resonance which is an electromagnetic analog to molecular orbital hybridization [13]. The model assumes that a complex structure's plasmon resonance will be a hybrid of the structures basic components. For example, a dielectric core with a gold shell could be modeled as the hybridization of a spherical cavity in an

infinite gold plate and a gold sphere as shown in Figure 14.

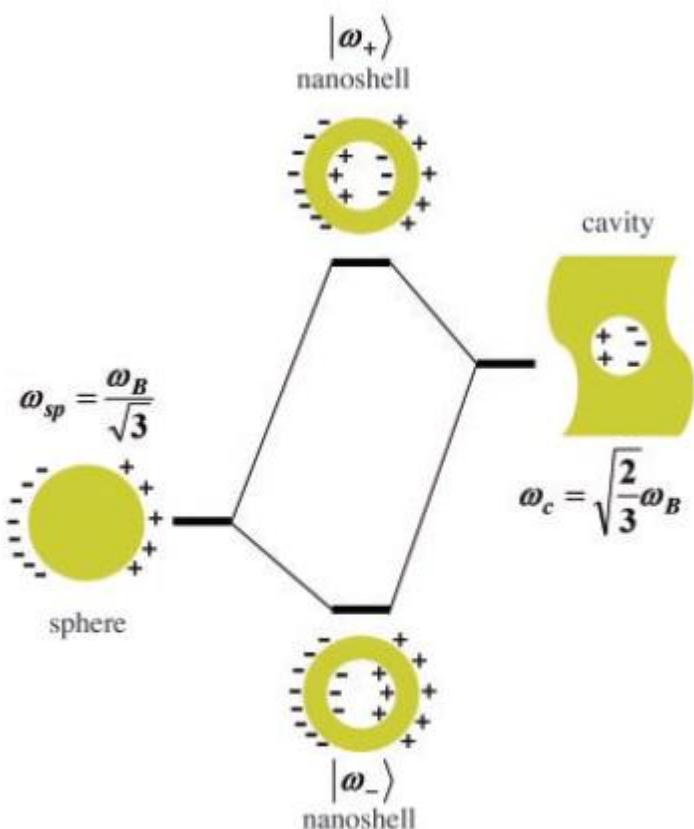


Figure 14: A hybridization model analogous to molecular orbital theory for predicting the plasmonic behavior of complex nanostructures such as core/shell configurations. Figure taken from [13].

Following this model, researchers have characterized many non-symmetrical shapes such as nanocups, nanoeegs, and offset cores in multi-layered core-shell structures [14].

## Section VI: Conclusion

This review has outlined the basics of optical properties as they apply to noble metals including the origin of optical properties, advanced band structure diagrams, and experimental determination of optical constants. In addition, this review outlined the localized surface plasmon resonance which forms the foundation for the emerging field of plasmonics. This new and exciting field has taken advantage of the optical properties of noble metals at the nanoscale to give rise to novel applications and technologies.

## Works Cited

- [1] "Electronic Band Structure," Wikimedia, 23 April 2012. [Online]. Available: [http://en.wikipedia.org/wiki/Electronic\\_band\\_structure](http://en.wikipedia.org/wiki/Electronic_band_structure). [Accessed 30 April 2012].
- [2] H. Ehrenreich and H. R. Philipp, "Optical Properties of Ag and Cu," *Physical Review*, vol. 128, no. 4, 1962.
- [3] "Brillouin Zone - Wikipedia," Wikimedia, 13 December 2011. [Online]. Available: [http://en.wikipedia.org/wiki/Brillouin\\_zone](http://en.wikipedia.org/wiki/Brillouin_zone). [Accessed 15 April 2012].
- [4] B. Segall, "Fermi Surface and Energy Bands of Copper," *Physical Review*, vol. 125, no. 1, pp. 109-122, 1962.
- [5] M. Suzuki and I. S. Suzuki, "Lecture note on Solid State Physics," in *State University of New York at Binghamton*, Binghamton, 2006.
- [6] C. B. Sommers and H. Amar, "Relativistic Band Structure of Gold," *Physical Review*, vol. 188, no. 3, 1969.
- [7] A. Sekiyama, J. Yamaguchi, A. Higashiya, M. Obara, H. Sugiyama, M. Y. Kimura, S. Suga, S. Imada, I. A. Nekrasov, M. Yabashi, K. Tamasaku and T. Ishikawa, "The Prominent 5d-orbital contribution to the conduction electrons in gold," *New Journal of Physics*, vol. 12, 2010.
- [8] "Willet's Lab Concepts: LSPR," University of Texas, [Online]. Available: <http://willets.cm.utexas.edu/LSPR.html>. [Accessed 25 April 2012].
- [9] S. K. Ghosh, S. Nath, S. Kundu, K. Esumi and T. Pal, "Solvent and Ligand Effects on the Localized Surface Plasmon Resonance (LSPR) of Gold Colloids," *Journal of Physical Chemistry B*, vol. 108, pp. 13963-13971, 2004.
- [10] H. Wang, F. Tam, N. K. Grady and N. J. Halas, "Cu Nanoshells: Effects of Interband Transitions on the Nanoparticle Plasmon Resonance," *Journal of Physical Chemistry B Letters*, vol. 109, pp. 18218-18222, 2005.
- [11] K. Aslan and C. D. Geddes, "Directional Surface Plasmon Coupled Luminescence for Analytical Sensing Applications: Which Metal, What Wavelength, What Observation Angle?," *Analytical Chemistry*, vol. 81, pp. 6913-6922, 2009.
- [12] S. Lal, S. Link and N. J. Halas, "Nano-Optics From Sensing to Wave Guiding," *Nature Photonics*, vol.

12, 2007.

- [13] E. Prodan, C. Radloff, N. J. Halas and P. Nordlander, "A Hybridization Model for the Plasmon Response of Complex Nanostructures," *Science*, vol. 302, pp. 419-422, 2003.
- [14] J. Qian, W. Wang, Y. Li, J. Xu and Q. Sun, "Optical Extinction Properties of Perforated Gold-Silica-Gold Multilayer Nanoshells," *The Journal of Physical Chemistry C*, 2012.
- [15] Y. Li, X. Liu and Z. Lin, "Recent Developments and Applications of Surface Plasmon Resonance Biosensors for the Detection of Mycotoxins in Foodstuffs," *Food Chemistry*, vol. 132, pp. 1549-1554, 2012.